Fabrication and characterization of single-crystal diamond photonic cavities

a dissertation presented
by
Jonathan Lee
to
The School of Engineering and Applied Sciences

in partial fulfillment of the requirements
for the degree of
Doctor of Philosophy
in the subject of
Engineering Sciences

Harvard University
Cambridge, Massachusetts
May 2013

Thesis advisor: Evelyn L. Hu Jonathan Lee

Fabrication and characterization of single-crystal diamond photonic cavities

Abstract

Cavity quantum electrodynamics provide a platform to form a quantum network which connects individual quantum bits (qubits) via photon. Optical cavity, a device which traps photons in a confined volume can enhance the interaction between photons and the qubits serves as fundamental building block for a quantum network. Nitrogen vacancy (NV) centers in diamond has emerged as one of the leading solid-state qubits because of its long spin coherence time and single photon emission properties at room temperature. Diamond optical micro-cavities are highly sought after for coupling with NV centers. Fabrication of optical cavities from nano-crystalline diamond film has been demonstrated previously. The quality factor (Q) of such devices was limited by the material properties of the nano-crystalline diamond film. Fabrication of single-crystal diamond photonic cavities is challenging because there is no trivial way to form thin diamond film with optical isolation. In this thesis, we describe an approach to fabricate high quality single-crystal diamond optical cavities for coupling to NV centers in diamond.

Single-crystal diamond membranes were generated using an ion-slicing method. Whispering gallery modes were observed for the first time from microdisk cavities made from such material. However, the cavity Q ($\sim$ 500) was limited by the ion damage created during processing. By using an homo-epitaxial overgrowth method, a high quality diamond film can be grown on the ion damaged mem-

branes. Microdisk cavities with Q $\sim$ 3,000 were fabricated on these improved materials. Diamond membranes with a delta-doped layer of NV can be made using a slow overgrowth process which demonstrate the position and density of NV centers can be controlled in these membranes. Photonic crystal cavities with Q $\sim$ 4,000 were fabricated from the delta-doped membranes with cavity resonance near the zero phonon line of NV centers. Different color centers can also be introduced during the overgrowth process, and optical coupling of an ensemble of silicon vacancy centers is demonstrated by coupling to a diamond microdisk cavity. We believe the techniques developed in this thesis could contribute to building of a quantum photonic network using diamond as a platform.

Contents

Author List

The following authors contributed to Chapter 1: Patrick Malentinsky, Sungkun Hong, Evelyn L. Hu

The following authors contributed to Chapter 2: Andrew P. Magyar, Igor Aharonovich, Fabian Rol, Menbing Huang, David R. Clarke, Evelyn L. Hu

The following authors contributed to Chapter 3: Igor Aharonovich, Andrew P. Magyar, Bob B. Buckley, Christopher G. Yale, David D. Awschalom, Evelyn L. Hu

The following authors contributed to Chapter 4: Kenichi Ohno, Igor Aharonovich, Andrew P. Magyar, David Barcher, Ania Bleszynski Jayich, David D. Awschalom, Evelyn L. Hu

The following authors contributed to Chapter 5: Kenichi Ohno, Claire McClellan, David O. Bracher, Ania Bleszynski Jayich, David D. Awschalom, Evelyn L. Hu

The following authors contributed to Chapter 6: Igor Aharonovich, Evelyn L. Hu

Listing of figures

This work is dedicated to my family.

Acknowledgments

This thesis would not have been finished without helps from many people, in the following paragraphs, I would like to acknowledge the people who have helped making this research project possible and those who have enriched my life during my short research career.

The first person I would like to acknowledge is my advisor, Evelyn Hu. Evelyn is an advisor that any graduate student could dream for. I really appreciate her patience and constant support through out my graduate school career especially when things do not go well, also the fact that she cares more about developments of the students more than research results. I thank Evelyn for being a great role model and for all the gifts, foods and birthday cakes. Lastly, I thank her for getting a group of talented and awesome people together which really makes my experience in graduate school worth so much more.

Chiou-Fu Wang is my first mentor and he has led me into the Hu group. I have the fortunate to know Chiou-Fu since freshmen year and he has always been a great friend and giving me insightful advises in both science and life. Chiou-Fu has started the diamond photonics projects in our group and taught me many fabrication techniques. Those days working with Chiou-Fu are still the most memorable time of my research career. This thesis is only partially fulfilling what Chiou-Fu and Evelyn have envisioned. I sincerely thanks your for your guidance and friendship.

I would also like to thank a special group of people who have moved from the sunshine California to the northeast part of this country with me. First, I would

like to thank Tsung-li Liu and his wife, Yvonne Kuo. Tsung-li and Yvonne take me as their roommate and indulge me with all the lunch boxes and home-cooked dinners that make me feel at home. Tsung-li is one of the smartest person I have met, his insights have helped clarified many concepts from semiconductor physics to optics. I thank Tsung-li and Yvonne for making me appreciate the small joys in life. John Joo is one of the most stubborn person I have ever met in my life. John is also a man who serves the community, without his persistence and efforts, our lab would not be as cleaned and organized. His stubbornness, persistence and boundless enthusiasm make him a great lab mate, a great defender in basketball games and a great friend. I thank John for spending many late nights together in the lab. I would also like to thank Fabian Rol, the most gentle person I have met. Fabian is my second mentor in the lab, we have worked together for a little bit more than a year on the diamond project. Fabian's creativity and courage have led to the fabrication of the diamond membranes. I thank Fabian for letting me realize good research is not only by careful planning but also by trying different things. Alex Woolf also moves from UCSB with us and he has helped building up some of the key components in our lab including the gas injection tube in the cryo-stat.

I feel fortunate to be with a group of people who love science and also care about others in the lab. Kasey Russell is one of the first person I have met in Harvard. Venky has once told us that it is very lucky for us to get Kasey which I cannot agree more after working with Kasey for four years. Kasey is the leader in this group because his enthusiasm toward science which influences people around him. Kasey also does a lot of work that could not be seen on record which enables almost all the projects in our group. Shanying Cui always bring a lot of energy and joys to the lab. I thank Shanying for making the lab a joyful place and her efforts in revising my thesis. Nan Niu is a man with many talents. I thank Nan for all the good time hanging out in or out of the lab during late night. Andrew Magyar and I have been working together for more than three years on the diamond projects. I thank Andrew for teaching me a lot of experimental tricks and this thesis would not have been completed without your efforts. I also work very closely with Igor Aharonovich on the diamond project for two years. Igor's immediate arrival to the

group propels the diamond project. I thank Igor for being a nice complementary in the diamond team and for all the help I have received from him. David Bracher and I have worked together for the past year on the diamond photonic projects and developing processing for SiC cavities. I want to thank David for all the hard work he puts into these projects while taking and teaching classes. I first know Katie and Christine as their TF and I am really happy to see both of them join the Hu group. I thank Katie for her effort on revising my thesis. I also thank Christine for being an energetic and cheerful office mate. I give my best wishes to the four first year graduate students, Andy Greenspon, Tina Huang, Dangqing Wang, and Alex Zhang. I would also thank all the Hu group alumni, Elaine, Ridah, Yong-Seok, Juan, Kevin, Adele, Kelly, Liz and David who all give me help when I started my graduate school career at UCSB.

I also thank my committee members, Professor David Clarke, Professor Marko Loncar and Professor Robert Westervelt for the valuable inputs they provide to my thesis. I especially thank Professor Clarke for letting us using the confocal microscope and all the other equipments in his lab.

I have the fortunate to have many wonderful collaborators during graduate school. I would like to thank Professor David Awschalom and Professor Ania Bleszynski Jayich for their supports. I would also like to thank Bob Buckley and Chris Yale for doing the spin coherence measurements and hosting me during summer 2011. I also thank Bob for his efforts on the initial characterizations on the microdisk samples using the lifted-off membrane and on the suspended cavities. Kenichi Ohno and Claire McLellan have been instrumental in the delta-doped membrane projects. I also thank Joseph Heremans, Benjamin Aleman, Abram Falk, Greg Fuchs, David Toyli and Paolo Andrich for all the help I received from them. Patrick Malentinsky and Sungkun Hong in the Yacoby's group have kindly helped us do the initial ESR characterization on the lifted-off membranes.

There are also many friends outside the group who makes my life more colorful. I thank Yinan Zhang for sharing his wisdom with me through many inspiring conversations. Birgit Hausmann, Jennifer Choy and Tom Babinec have all provided many helps which makes the transition to Harvard much easier. Raji Shankar, Yu-

Ting Lin, Qimin and I-Chun have been very good floor mates to hang out with. I also thank my office mates on the third floor, Shota, Cheng, Ray, and Yang. I thank all the teammates in the Harvard Taiwanese student basketball team including Jeff, Yang-Ting, Kevin, Michael, Eric, Kuo-Hua, Che-Hang, Li-Hsing and David for all the weekend basketball games.

My families have always been very supportive on my decisions. I thank them for their unconditional love and supports. I would like to thank my father for always having faith in his son. I thank my mom for her constant encouragements and providing an environment that is full of love for me and my sister. I thank my sister for always giving me her most honest opinions. I also thank my grandparents for sharing their wisdom with me and encourage me to pursue knowledge. I want to thank my dog Chucky for being with my parents when me and my sister are away from home. We will always miss you. Lastly, I would like to thank my wife, Jennifer Chen. The long distance relationship could be difficult to maintain but I am glad that we will get through it soon. I thank my wife for her supports and understanding on all the decisions I have made and I look forward to start our journey of life together.

1

Introduction

1.1 Overview

The negatively charged nitrogen vacancy (NV) centers in diamond have emerged as a leading physical system for solid-state quantum information processing (QIP) [1, 2]. The NV center possesses many extraordinary physical properties: it has a long electron spin coherence time [3], its ground state electron spins can be op-

tically read out and polarized, and it could be the basis of a single photon source [4, 5]. Most importantly all the above properties hold true at room temperature. Recent demonstrations of coherent manipulation of ground state electron spins [6], spin-photon entanglement [7], two photon interference [8, 9] and entanglement of distant spins in diamond [10] further motivates building of a quantum photonic network to entangle distant NV centers in diamond [2, 11, 12].

Several technological challenges need to be overcome in order to build a quantum photonic network using NV centers. First, efficient collection of photon from NV centers is required. Second, modification of intrinsic emission properties of NV centers allows more photons to be emitted. Third, positioning the NV centers with high spatial resolution within an optical cavity is crucial for scaling up the quantum network. The first two challenges could be circumvented by shaping materials into different photonic structures, which has been demonstrated in III-V semiconductor materials [13]. The third task is very challenging even in more mature solid-state system (e.g. self-assembled quantum dots in III-V semiconductors [14]). However, recent breakthroughs in diamond growth and material processing may shed light on overcoming such challenges[15, 16].

In this thesis, we focus on developing fabrication techniques to make high quality diamond photonic cavities [17]. An ion-slicing method was developed to fabricate single-crystal diamond membranes [18]. Photonic cavities with quality factors up to a few thousand were fabricated by improving the membrane quality using growth techniques [19]. Combining with diamond overgrowth methods, the approach presented in this thesis provides an opportunities to fabricate integrated

photonic network with NV centers in controlled positions.

1.2 NV centers in diamond

Diamond is a material with extreme material properties. It is well known for its hardness which makes it popular as a cutting tool. Its bio-compatibility and chemical inertness makes diamond an attractive material for bio-sensing applications [20–22]. It is a semiconductor with a wide electronic band gap $\sim$ 5.5 eV which makes it suitable for high power operations. Diamond also has a high thermal conductivity which makes it a good heat sink material. Besides all these extreme qualities, diamond is also a material host of more than 100 different defect centers that emit light [23]. Many of these color centers have attracted much attention in recent years as solid-state based single photon emitters [24], such as the NV centers [4, 5], the silicon vacancy (SiV) centers [25] and the chromium centers [26]. In this section we will focus on the negatively charged NV centers in diamond which have been most heavily investigated out of all these color centers because of their unique spin properties.

The NV centers in diamond consist of a substitiutional nitrogen atom with a neighboring vacancy site in the diamond lattice, as shown in Figure 1.2.1(a). The NV centers have a symmetry axis along the <111> crystal axis. The NV centers could be in two different charged state, the negatively charged state (NV^-) or the neutrally charged state (NV^0). In the remainder of this thesis we refer to the negatively charged state as the NV center. The NV center is commonly modeled with six electrons; three electrons from the adjacent carbon atoms, two from the sub-

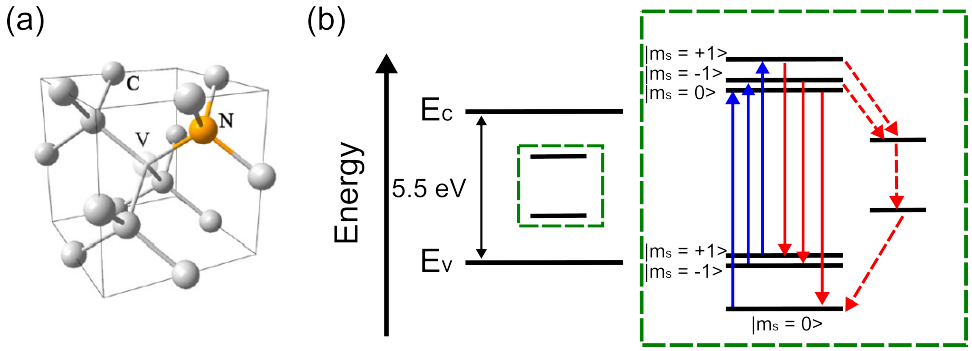

Figure 1.2.1: (a) The negatively charged Nitrogen-vacancy centers consist of subsitutional nitrogen with a neighbor vacancy site in a diamond lattice. (b) The ground state of NV centers is a spin triplet, the excited states are$\sim$ 1.945 eV above the ground state. There is a singlet dark state in between the ground states and the excited states which is responsible for the ISC and lead to ODMR and optical spin polarization. Figure 1.2.1(a) is adapted from [24] with permission.

stitutional nitrogen atom and an extra electron, making it negatively charged.

The electronic levels of NV centers are shown in Figure 1.2.1(b). The ground state of NV centers is a spin triplet with a zero-field splitting of 2.88 GHz between the spin state $m_S = 0$ and the spin states $m_S = \pm 1$, quantized along the symmetry axis, the <111> crystal axis [27]. The excited states are $\sim$ 1.945 eV above the ground state with a singlet dark state $\sim$ 40 meV below the excited states [28]. The energy of NV center ground state is 2.6 eV below from the conduction band and 2.94 eV above from the valence band which makes it well protected from thermal fluctuation even under room temperature environments [29].

1.2.1 Spin Properties

The first optically detected magnetic resonance (ODMR) measurement from NV centers was demonstrated in 1997 [30]. Figure 1.2.2 shows an ODMR dip measured from the NV centers in a bulk diamond grown via chemical vapor deposition (CVD). A 532 nm laser excitation is used to excite the electrons from the ground states of the NV centers to the excited states. The fluorescence signal is collected through a confocal microscope and sent to an avalanche photo-diode (APD). The spin state-dependent fluorescence contrast occurs because of the inter-system crossing (ISC), where the electrons in the excited states with spin states $m_S = \pm 1$ relax into the singlet dark state preferentially, compared to the excited states with spin state $m_S = 0$ [27, 31]. Since the optical excitation from the ground states to the excited states follows the optical selection rule (optical transition occurs only if $\Delta m_S = 0$), the photon emission rate for the optical transitions from the $m_S = \pm 1$ spin state is 10 times smaller compared to the transitions from the $m_S = 0$ state [32]. The fluorescence contrast can be observed when the electrons in the ground state are populated into the $m_S = \pm 1$ state by a microwave excitation. The ground state spins can be re-initialized by using a linearly polarized laser excitation which preferentially pumps the electrons in the ground state with spin state $m_S = 0$ [33].

There are many different spin relaxation mechanisms. In this thesis, three different relaxation times are used to characterize the spin properties of NV centers in the diamond membranes. The first one is the spin-lattice relaxation time (T_1) which characterizes the energy relaxation mechanism. The T_1 time determines

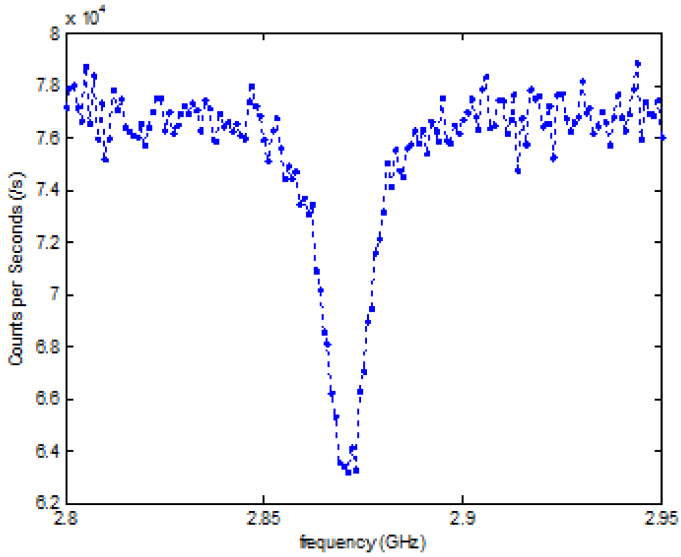

Figure 1.2.2: ESR dip could be observed from NV centers by applying an AC magnetic field with varying frequencies. When the frequency of the oscillating magnetic field was in resonance with the zero-field splitting of the ground state levels, electrons were populated in the $m_S = \pm 1$ state, reduced fluorescence from NV centers due to inter-system crossing (ISC) would occur and caused the fluorescence dip. This measurement was performed on a CVD diamond from Element Six^{TM} in Amir Yacoby's lab with Patrick Malentinsky and Sungkun Hong.

how long an electron can stay in the spin state and the change of spin state normally occurs through interactions with lattice vibration (phonons). The T_1 time sets the upper limit for the spin coherence time (T_2) which is a phase relaxation time. The T_2 time allow us to know how long the electron spin states can keep their phase for a single spin. The T_2 time can be measured from an ensemble of spins using the Hahn echo techniques by first letting the spin state freely precess for a given time τ then apply a π-pulse which turn the spins 180° about the axis normal to the plane of precession and let the spin freely evolve for time τ, therefore, the inhomogenous distribution of the precession rates for different spins will be compensated. The T_2 time needs to be much longer than the manipulation time of electron spin for quantum error correction [34]. The third relaxation time scale is the transverse inhomogeneous dephasing time (T_2^*) which is described in equation 1.1. The T_2^* determines how fast the phase of the spin randomized during free evolution. Therefore, the manipulation time needs to be greater than T_2^* for high fidelity control over the spin.

$$\frac{1}{T_2^*} = \frac{1}{T_2} + \frac{1}{T_{inh}} \tag{1.1}$$

Diamond is an ideal material host for the spin defects because the weak spin-orbit interaction and the nuclear-spin free environment (naturally abundant ^{12}C is 98.9%). Electron spin coherence time (T_2) on the order of 1 ms was observed at room temperature in a ^{12}C isotopically purified diamond [3]. Coherent manipulation of the ground state electron spins in a single NV center was first demonstrated in 2004 by using an oscillating magnetic field [6] and recently demonstrated by

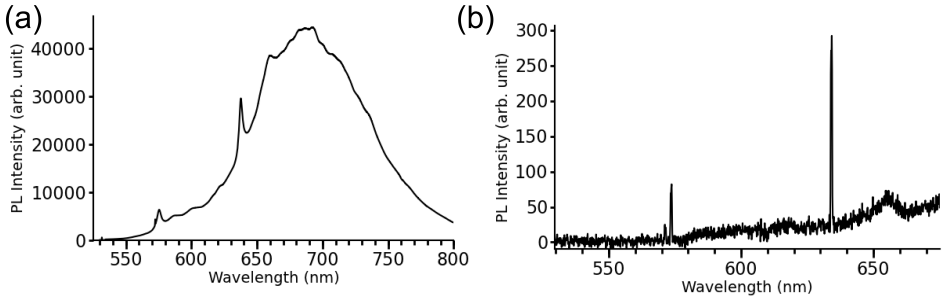

Figure 1.2.3: (a) The room temperature PL spectrum of NV centers measured using a confocal microscope with 532 nm laser excitation. The spectrum consists of a zero phonon line centered at 638 nm for the NV^- state and a broad phonon side band extended to 800 nm. (b) PL spectrum of NV centers was measured at 40 °K. ZPL of both NV° (centered at 575 nm) and NV^- (centered at 638 nm) were observed. Phonon side band was still observed even at low temperature.

using an optical field [35]. With these unique properties, the NV centers have attracted much more attention as a solid-state spin qubit.

1.2.2 Optical Properties

A single NV center could be imaged by collecting the photoluminescence (PL) signal from the NV center using a confocal microscope with 532 nm laser excitation [32]. The PL spectrum of the NV centers in diamond, shown in Figure 1.2.3, consists of a zero phonon line (ZPL) transition of negatively charged NV center (NV^-) centered at 638 nm and a broad phonon side band ranging from 638 nm until $\sim$ 800 nm. Even at low temperature, a significant amount of energy still goes into the phonon side band due to the good electron-phonon coupling (low branching ratio into ZPL, $\sim 4\,\%$ at 4 °K) which is shown in Figure 1.2.3(b). The fluorescence lifetime of NV centers is typically $\sim$ 13 ns.

1.3 Cavity QED

Much progress has been made in semiconductor micro-cavities, due to the rapid progress in semiconductor fabrication technology. Optical cavities with Q greater than 10^6 have been fabricated in fused silica [36]. Photonic crystal cavities with smaller modal volumes have been made to couple to a single self-assembled quantum dot [37].

1.3.1 Cavity: Figures of merit

The quality factor (Q) of an optical cavity is described as the energy dissipation per optical cycle [38]. The cavity Q determines how long photons can be trapped within the cavity. Optical loss is normally described by an exponential decay in time. Therefore, Q can be determined by looking at the full width at half maximum (FWHM) of the cavity mode resonance in the frequency domain, fitted by a Lorentzian profile (Equation 1.2).

$$Q = \frac{\omega_{cav}}{\Delta\omega_{cav}} \tag{1.2}$$

The ω_{cav} is the resonance frequency of the optical cavity and the $\Delta\omega_{cav}$ is the FWHM of the cavity mode resonance. The cavity Q can be limited by different loss mechanisms including scattering loss due to fabrication imperfection and the material re-absorption.

Another key figure of merit for an optical cavity is the modal volume (V) which

describes the spatial photon confinement in the cavity (Equation 1.3).

$$V_{mode} = \frac{\int_V \varepsilon(r)|E(r)|^2 d^3r}{max[\varepsilon(r)|E(r)|^2]} \tag{1.3}$$

The V_{mode} is the modal volume of the cavity mode. ε(r) is the permittivity of the material at a give position r. E(r) is the electrific field at a given position. The smaller the modal volume the stronger the interaction strength. For dielectric cavities, the modal volume is limited by the diffraction limit.

1.3.2 Weak coupling regime: Purcell enhancement

All of the emitters considered in this study have physical dimensions much smaller than the optical wavelength. Therefore, the dipole approximation is valid in general. The Purcell enhancement can be derived using time-dependent perturbation theory with the Hamiltonian of dipole interaction, $H = d \cdot E$, where d is the optical dipole moment of the emitter and E is the electric field [39]. The Purcell enhancement (F_P), which defines the change of spontaneous emission rate when the emitter is coupled to a cavity mode (Γ_{cav}) compared to the spontaneous emission rate in vaccum (Γ_o), can be expressed as the following equation 1.4 [40].

$$F_P = \frac{\Gamma_{cav}}{\Gamma_o} = \frac{3}{4\pi^2}\frac{Q}{V_{mode}}(\frac{\lambda_{cav}}{n})^3 \tag{1.4}$$

Where λ_{cav} is the resonance wavelength of the cavity mode, assuming the cavity mode has complete spectral overlap with the emitters it is coupling to. Additional factors need to be taken into account to determine the coupling strength between

the cavity mode and emitter, including: 1. spectral overlap, 2. spatial overlap, 3. dipole orientations [41]. Since the color center emission is normally fixed, the spectral overlap requires the cavity mode wavelength to be in resonance with the color center emission. In most cases, the positions of NV centers are randomly distributed within the sample, and therefore, spatial overlap between the cavity mode and a single NV center is by chance. In order to have maximum coupling, the dipole orientation needs to be parallel or anti-parallel to the electric field of the cavity mode.

1.4 Diamond Quantum Photonics

There has been much progress in fabricating photonic structures on diamond [12, 42–44]. Fabrication of nano-pillar structures [45] and solid immersion lens [46] from diamond have enabled 10-fold enhancement in photon collection efficiency from NV centers. In the mean time, single-shot readout of electron and nuclear spins from the NV centers with high fidelity have been demonstrated [47, 48]. With the fine tuning of the NV ZPL using the Stark effect [49], two photon interference from distant NV centers has been achieved [8, 9]. With engineered photonic structures and better control over the optical and spin properties of NV centers in diamonds, heralded entanglement of distant spins in diamond has been recently realized [10]. Such results promote the NV centers into one of the leading candidates for solid-state quantum information processing (QIP) [11, 50, 51].

Despite the many successful proof of principle demonstrations, there are still many technological challenges to overcome. First, even with the 10-fold enhance-

ment of photon collections from the engineered photonic structures, the NV centers still suffer from the low branching ratio ($\sim 4\%$) into the NV ZPL. One way to resolve this problem is by building diamond optical cavities to resonantly enhance the NV ZPL transition. Microdisk cavities and photonic crystal cavities have been fabricated from nano-crystalline diamond thin films [52, 53]. However, the cavity Q is limited mainly by the absorption from defects in the grain boundaries and the poor polycrystalline material quality. Therefore, fabrication of photonic structures from high quality single-crystal diamond material is desirable to improve the device performance. Fabrication of photonic structures out of single-crystal diamond still remains challenging. Until today, there has been no demonstration of heterogeneous growth of high quality single-crystal diamond over a large area (mm-scale). Such technological constraints limit the possibility to use a heterogeneous sacrificial layer to create a suspended air-dielectric-air geometry that is required for optical confinement. With the recent breakthrough in creating diamond membranes that are 5-20 μm thick using a laser ablation methods (from Element Six^{TM}), high Q cavities could be fabricated by thinning the diamond membranes down to few hundred nanometers [54–57]. Such breakthrough have enabled first demonstration of resonant enhancement of NV ZPL in membranes using micro-ring resonators [54], photonic crystal cavities [56], and integrated photonic structures [55, 57, 58].

Another challenge to scaling up the diamond photonic network is controlling the position of NV centers. There have been efforts on placing the NV centers with high spatial resolution through nitrogen implantation [15, 59]. However, the

quality of the NV centers degrades using such an approach, due to the ion damage. There has been a recent breakthrough by introducing a sheet of NV centers with good spin coherence properties in a controlled position by growing a nitrogen delta-doped layer on bulk diamond [16]. Such growth techniques have enabled magnetic field sensing of NMR signal from protons in an organic polymer [60]. Hopefully by controlling the position of the NV centers and by fabricating high quality diamond photonic devices, a quantum network could be built using a diamond chip.

1.5 Contribution and organization of this work

In this thesis, we developed processing techniques to fabricate high quality diamond cavities on single-crystal diamond membranes. The diamond membranes were fabricated using a variation of the ion-slicing method developed in the 1990's [61]. This technique produced suspended microdisk structures [62] and microring structures [63], but with no observation of optical modes. Such results, lead to our investigation which is described in chapter 2. By lifting off the diamond membranes from the bulk diamond, the material quality of the diamond membranes can be probed independently by using Raman spectroscopy and PL measurements. Through our study, the influence of ion damage to the diamond membranes is revealed by a broadened, shifted first order diamond Raman line [18]. Microdisk cavities were fabricated on the lifted-off membranes. Whispering gallery modes (WGMs) were observed for the first time using the ion-slicing approach and the cavity Q was limited to ~ 500, which is comparable to the microdisk cav-

ities made in nano-crystalline diamond film [52]. The cavity Q limitation was thought to be due to the ion damage during processing. This result led us to find other ways to improve the material quality of diamond membranes. In chapter 3, we describe a way to fabricate high quality diamond membranes by performing a diamond overgrowth on the lifted-off membranes using plasma-enhanced chemical vapor deposition (PECVD). The overgrown material showed a narrower Raman line ($\sim$ 2.5 cm^{-1}) compared to the ion damaged membranes ($\sim$ 9.9 cm^{-1}). Microdisk cavities fabricated from the overgrown material showed higher Q ($\sim$ 3,000) compared to the cavities fabricated from the ion damaged membranes. These encouraging results further allowed the demonstration of high quality photonic devices using the ion-slicing method.

Strong NV luminescence was observed from the overgrown membranes. The spin properties of NV centers in the overgrown membranes was characterized by Bob Buckley and Christopher Yale in David Awschalom's lab at UCSB. The T_2 spin coherence time observed ($\sim 3\mu s$) was good for ensemble measurement. SiV centers can also be incorporated during the growth by placing diamond membranes on a different holding substrate (e.g. Si). With the improved cavity performance and incorporation of the SiV centers, evidence of optical coupling of WGM (Q$\sim$ 2,500) with the SiV centers was observed from a diamond microdisk cavity.

In order to couple the cavity mode with a single NV center, the NV density needs to be controlled. In chapter 4, in collaboration with the UCSB group, diamond membranes were grown with and without introduction of nitrogen. The un-doped membrane exhibited no NV fluorescence and a Raman linewidth as

narrow as the bulk CVD diamond. From the nitrogen-doped membranes, strong NV fluorescence was observed. This demonstrated that NV density could be controlled by adjusting growth conditions using a good PECVD reactor. Microdisk cavities with $Q \sim 2{,}900$ were fabricated on the un-doped membranes suggesting high quality photonic devices could be made from these tailor-made membranes. With recent advances in diamond growth techniques, diamond membranes with a ^{15}N delta-doped layer were grown on ion-implanted bulk diamond substrate by Kenichi Ohno at UCSB. The ^{15}N delta-doped membranes exhibited narrow Raman characteristics and NV fluorescence. In chapter 5, undercut photonic crystal cavity structures were fabricated by bonding the diamond membranes to PMMA. Photonic crystal cavities with $Q \sim 4{,}000$ and $V \sim 0.47\ (\lambda/n)^3$ were fabricated on the ^{15}N delta-doped membranes. This result proves that high quality devices could be fabricated from the engineered material.

We believe the process techniques developed in this thesis pave the way to fabricate high quality diamond membrane with predetermined NV position. This could lead to building a platform for integrated quantum network using NV centers in diamond.

2

Fabrication and characterization of single-crystal diamond membranes

2.1 Introduction

Microdisk cavities and photonic crystal cavities have been fabricated from nanocrystalline diamond thin film [52, 53]. However, the cavity Q is limited mainly by

the absorption from defects in the grain boundaries and the poor material quality due to its polycrystalline nature. Therefore, fabrication of photonic structures from high quality single-crystal diamond material is desirable to improve the device performance. Fabrication of photonic structures out of single-crystal diamond still remains challenging. Until today, there has been no demonstration of heterogeneous growth of high quality single-crystal diamond. Such technological constraints limit the possibility to use a heterogeneous sacrificial layer to create a suspended air-dielectric-air geometry that is required for optical confinement. A promising approach to make high quality diamond photonic devices is to fabricate single-crystal diamond membranes that are few hundred nanometers thick using ion slicing methods [61, 64]. The single crystal diamond membranes can be put on a dielectric substrate with lower refractive index compared to diamond in order to preserve the optical confinement.

In this chapter we describe the experimental studies on the material quality of single-crystal diamond membranes fabricated using the ion slicing method. Diamond membranes with ~ 1.7 μm thickness were fabricated first using ion implantation with sufficient ion dose to create a heavily damaged layer buried in diamond. The heavily damaged layer was then selectively removed using an aqueous electrochemical process that has been reported previously [62]. The diamond membranes were lifted off by complete removal of the heavily damaged layer and subsequently transferred to different dielectric substrates for device fabrication or optical characterization. The influence of the ion damage to the diamond membranes was characterized using Raman and micro-photoluminescence (μ-PL) measure-

ments. By etching different sides of the diamond membranes, the regions that experienced different amounts of ion damage can be characterized independently [18]. The near surface diamond membrane experienced less ion damage and showed bright NV-like luminescence and narrower first order diamond Raman line (~ 10 cm^{-1}) compared to the more damaged layer. However, the first order diamond Raman line was still broader compared to bulk diamond and no electron spin resonance (ESR) signature of NV centers was observed from the diamond membranes. Whispering gallery modes (WGM) were observed from microdisk cavities fabricated from the lifted off diamond membranes, where the more damaged layer was etched away. Microdisk cavities fabricated from such diamond membranes showed $Q \sim 500$. Further improvement of the cavity Q can be made by improving the material quality of the diamond membranes.

2.2 Fabrication of diamond membranes

2.2.1 History using ion slicing method

Fabrication of large sheet of single-crystal diamond membranes (mm-scale in lateral dimension) from bulk diamond samples was first demonstrated in the 1990's using a high energy (4-5 MeV) ion implantation followed by a thermal annealing process [61]. The high energy ions penetrate into the diamond lattice and create a heavily damaged layer near the end of the ion range via nuclear collision processes [65]. It is known that once the ion dose exceeds a certain threshold (critical dose), the ion damaged layer exhibits a mixture of sp^2 and sp^3 bonding upon thermal

annealing [66]. The ion range and critical dose are determined by implantation energy, ion dose, ion species, and implantation temperature. The ion damaged layer could be selectively removed using various methods including electrochemical etching [64], oxygen annealing [61, 67]and boiling acid treatment [61].

Different photonic structures have been fabricated using the ion slicing methods. Suspended optical waveguide structures were fabricated by first using a high energy (2 MeV) helium ion implantation to create the heavily damaged layer, then focused ion beam (FIB) patterning, followed by selective etching using boiling acids [68]. Because of the high energy and light mass ions that were chosen, the damaged layer was ~ 3.5 μm below the surface which left the device layer too thick for single mode operation. Thin diamond micro-rings ($\sim$ 200 nm) were fabricated using double helium implantations (1.8 MeV and 2.0 MeV) to create a thin layer sandwiched between two ion damaged layers that were $\sim$ 200 nm apart [63]. However, no optical resonance was observed from those devices. Suspended microdisk structures were fabricated on a 180 KeV Boron implanted bulk diamond ($\sim$ 150 nm below surface) followed by an overgrowth of $\sim$ 295 nm thick diamond epitaxial layer. Undercuts were made by selective removal of the heavily damaged layer using an electrochemical etching process [62]. With the overgrown process, a high quality diamond layer was expected to grow on the device layer, however, no optical resonance was observed. Two reasons were suspected: one, the ion damage in the microdisk degraded the optical performance of the devices; second, the short ($\sim$ 100 nm) cavity-substrate separation compromised the light confinement due to evanescent coupling of the cavity field to the substrate. Multiple implanta-

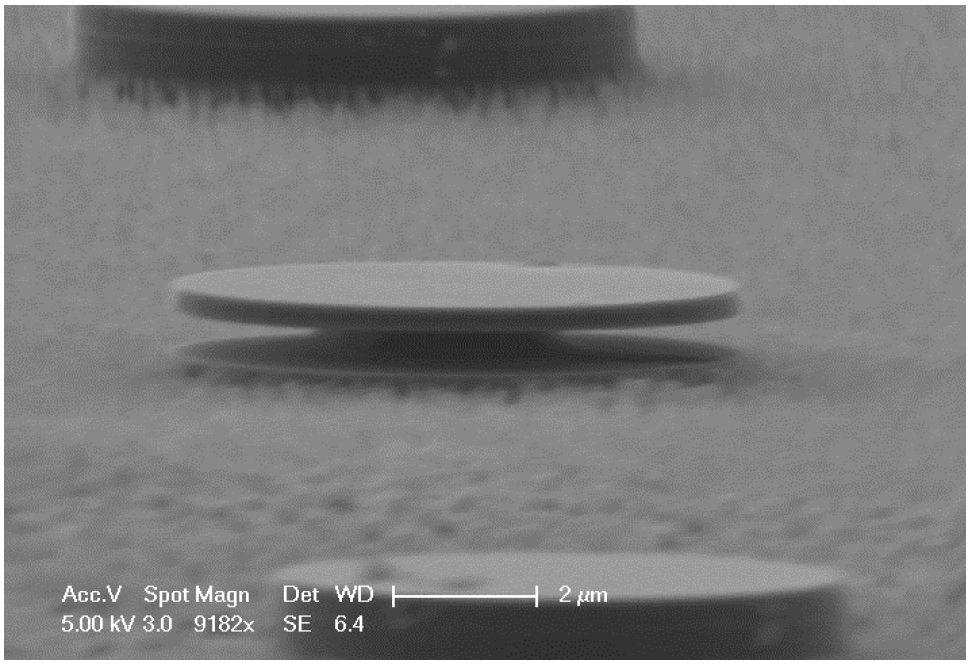

Figure 2.2.1: Microdisk resonators with large cavity-substrate separation ($\sim$ 700 nm) was fabricated. Four carbon ion implantation were applied to the bulk substrate with implantation energies 385 KeV, 700 KeV, 850 KeV and 1 MeV . The sample was annealed at 950 °C for 2 hours under nitrogen flow. An electrochemical etching was used to undercut the structure.

tions were explored to increase the cavity-substrate distance to $\sim$ 700 nm, and no optical cavity mode was observed. A scanning electron microscope (SEM) image of the suspended microdisk resonators are shown in Figure 2.2.1.

All the efforts described above demonstrated that ion slicing could be used to fabricate photonic structures. But the fact that no optical resonance was observed lead us to investigate the optical properties of the device layer alone. In order to measure the device layer alone, we went back to the initial approach developed in the 19990's, lifting off the diamond membranes.

2.2.2 Process flow

Figure 2.2.2 depicts the process flow to fabricate diamond membranes from bulk diamond samples using the ion slicing method. Diamond membranes were formed from a type IIa chemical vapor deposition (CVD) diamond sample with dimensions 4 mm $\times$ 4 mm $\times$ 0.5 mm and (100) crystal orientation purchased from Element Six ^{TM} with nitrogen concentration < 1ppm which still has substantial NV luminescence. The first step was creating a heavily damaged layer in bulk diamond using a 1MeV helium ion beam, with a dose of 5×10^{16} He^{+}/cm^{2} and an ion current of 2 μA (UDH tandem accerlerator ion implanter, National Electrostatics Corp.). Ion implantation was performed at 7° to normal angle to avoid ion channelling. Post implantation samples were annealed for 2 hours at $950^{\circ}C$ under nitrogen flow to facilitate the electrochemical etching/lift-off [69]. Photolithography was used to pattern a $\sim$ 200 nm thick SiO_2 hard mask, deposited by plasma-enhanced chemical vapor deposition (PECVD) (Surface Technology Systems). The mask patterns was etched into the diamond sample using oxygen inductively coupled plasma reactive ion etching (O_2-ICP-RIE) (Unaxis Shuttleline), yielding 250 μm square mesas. An electrochemical etching process was used to selectively remove the heavily damaged layer by using two tungsten probe tips in ultra-pure water (Millipore) under a DC voltage bias at least 10V [62, 70]. The positively biased tip contacted the heavily damaged region while the negatively biased tip was positioned slightly above the substrate (Figure 2.2.2). The electrochemical etch enabled the removal of individual diamond mesas (membranes), which were collected in a water droplet and transferred to a SiO_2-on-Si substrate via drop-casting.

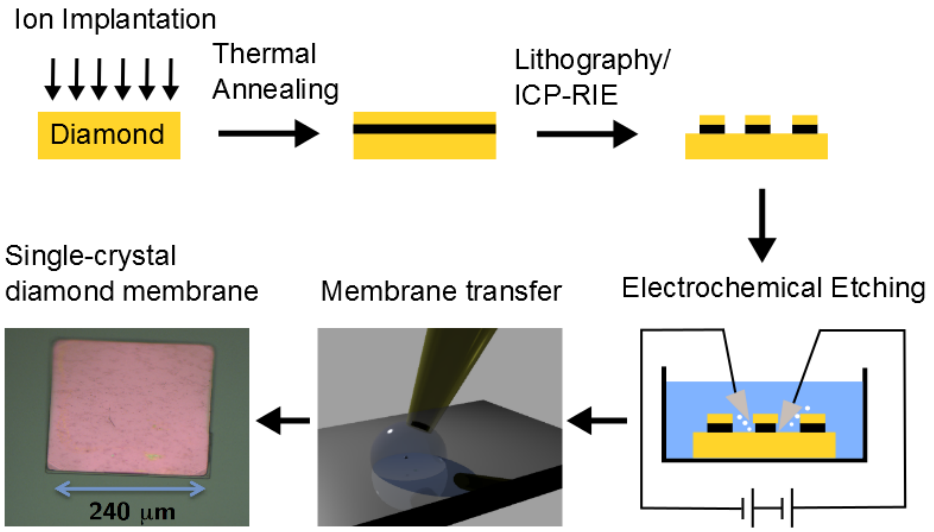

Figure 2.2.2: To fabricate single-crystal diamond membranes, the ion damaged layer was first defined by ion implantation followed by thermal annealing at 950 °C for 2 hours. The samples were patterned into mesas using photo-lithography and inductively coupled plasma reactive ion etching using SiO_2 as hard mask. The ion damaged layer was selectively removed using electro-chemical etching. The membranes were transferred to low index dielectric substrate by drop-casting using a pipette tip. Optical microscope image of the diamond membranes with dimension 250 μm $\times$ 250 μm were shown.

An optical micrograph of a lifted off membrane (250μm $\times$ 250μm $\times$ 1.7 μm) is shown in Figure 2.2.2.

2.2.3 Implantation damaging process

The implantation energy (1 MeV) and helium ion was chosen in our experiments to minimize ion damage near the surface, because the lighter mass of the helium ion allowed it to penetrate deeper into the diamond lattice. A Monte Carlo based software program, Stopping Range of Ion in Matters (SRIM), was used to predict

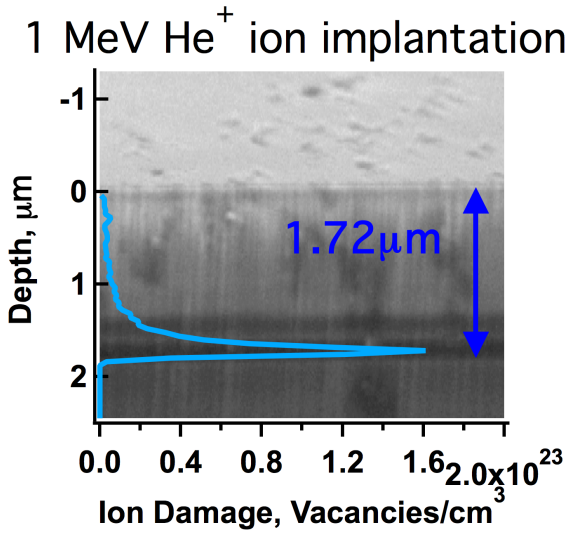

Figure 2.2.3: The position of the ion damaged layer could be predicted by SRIM simulation. The ion damaged layer was created by a 1MeV helium ion beam with ion dose 5×10^{16} He^{+}/cm^{2}. The dark layer in the SEM viewgraph was the ion damaged layer, its position agreed with the vacancy distribution calculated by SRIM simulation.

the ion damage (vacancies) profile. Figure 2.2.3 shows a comparison between the experimental observed position of the heavily damaged layer compared to the ion damage profile based on SRIM simulation. The location of the heavily damaged layer can be seen using SEM. The good agreement between the ion damage profile based on SRIM simulation and the experimental observation suggests that the ion damaged layer is ~ 1.7 μm into the diamond surface. This result also shows that SRIM simulation can be used to predict the position of the ion damaged layer which determines the thickness of the diamond membranes.

Diamond membranes with different thicknesses can be fabricated by choosing the ion species and the implantation energy. SRIM simulation provided an estima-

tion of the position of the heavily damaged layer which determines the thickness of the membranes. Although there have been several demonstrations of membrane lift-off using the ion slicing method and even on the influence of ion damage using cross section Raman measurements [71], there has been no study on the influence of ion damage on the lifted off membranes alone. In the next section we will describe the optical characterization performed on the lifted-off membranes.

2.3 Influence of ion damage on diamond membranes

Raman and PL spectra of the membranes were collected using 532 nm laser excitation in a confocal Raman microscope (LabRAM ARAMIS, Horiba Jobin-Yvon) with typical spatial resolution on the order of 1 μm, but with confocal depth of focus greater than the membrane thickness. The membranes were strongly fluorescent, exhibiting a broad emission band centered at about 677 nm. The PL is similar to that of the bulk diamond, but without the characteristic signature of the NV^- center, shown in Figure 2.3.1(b). The position and width of the first order diamond Raman line can provide information about residual stresses and ion damage [71] in the diamond membranes. The bulk diamond sample exhibited a Raman line centered at 1333.5 ± 0.1 cm^{-1} with a full-width half-maximum (FWHM) of 2.3 ± 0.1 cm^{-1}. The Raman spectrum of the membrane, shown in Figure 2.3.1(c), exhibited a broad peak (FWHM = 13 ± 1 cm^{-1}) centered at 1329.6 ± 0.1 cm^{-1} which is best fit with two peaks (see Figure 2.3.3). From the shifted Raman signal it is apparent that there is residual optical and structural damage in the diamond membranes. To remove the most heavily damaged material,

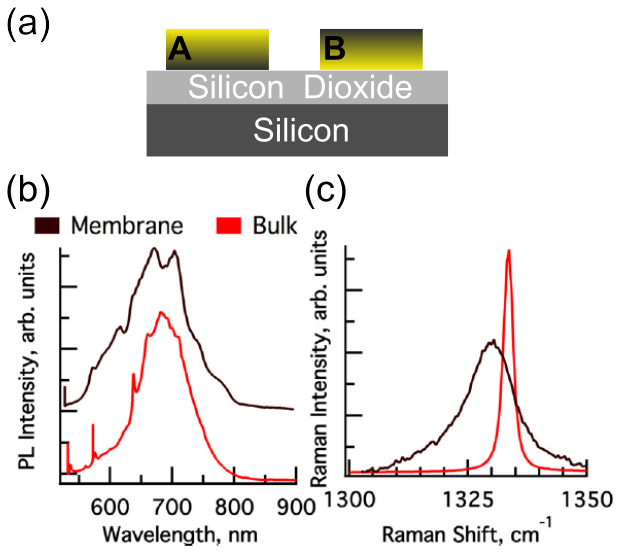

Figure 2.3.1: (a) Mesas are lifted off the substrate via electrochemical etching and transferred to a Si substrate coated with 1 μm SiO_2. Sample A is oriented with the damaged material on the surface, and sample B is oriented with the damaged material facing the SiO_2/Si substrate. (b) Luminescence and (c) Raman signals from lifted-off membrane (black) and bulk diamond (red).

the diamond membrane was systematically thinned by an O_2-ICP-RIE process. In order to gain more insight into the distribution of the damage within the membranes, we compared samples that were flipped, placing the most heavily damaged material at the surface (A), to samples where the exposed surface was the original surface of the bulk diamond (B), as depicted in Figure 2.3.1(a). These membranes were incrementally thinned by O_2-ICP-RIE, resulting in thicknesses of 800, 400, and 200 nm, respectively. The membranes were etched in 30 sccm of O_2 at 5 mTorr pressure; the O_2-ICP-RIE power was 600 W and the bias power was 100 W.

After each thinning step, Raman and PL spectra were recorded to study the damage and optical emission from A and B. Prior to thinning, the PL and Ra-

man signatures were similar for the unthinned samples A and B. As sample A was thinned, removing the most heavily damaged material, the PL spectrum more closely approached that of the bulk diamond. Figure 2.3.2 shows the room temperature PL spectrum of sample A, thinned to 200 nm. Given the changes in the total volume of material being excited, the total luminescence of the thinned sample was commensurate with that of the unthinned sample. The spectral signature of the NV-center, with peaks at 576.1 (FWHM: 7.0 nm) and at 641.1 nm (FWHM: 6.3 nm), corresponding to the neutral and the negatively charged NV centers was clearly observed. Also evident are the peaks corresponding to phonon replicas of the 641.1 nm NV^- ZPL present at 662.9, 682.5, and 713.1 nm, each separated by close to the 65 meV energy phonon in diamond. In contrast, the corresponding thinned 200 nm sample B membrane showed luminescence intensity decreased by about 2 orders of magnitude, compared to the unthinned sample.

The Raman peak for the unthinned membranes was best fit with two Voigt curves with a linear baseline: one centered at 1327 ± 0.1 cm^{-1} (designated low wave number, LWN) and the other at 1330 ± 0.3 cm^{-1} (designated high wave number, HWN), seen in Figsure 2.3.3(a) and (b). The optimal fit to two peaks may arise from the overlapping Raman signatures of the material closest to the peak of the implantation damage and also the material at the surface, furthest from the peak damage. As membrane A is thinned, the Raman signal collapses to a single peak at 1331.0 ± 0.2 cm^{-1} with a 9.9 ± 0.4 cm^{-1} FWHM, approaching the peak position and linewidth of bulk diamond, shown in 2.3.3(a). After etch removal of about 1 μm of sample A, there is no longer a LWN component of the Raman spectrum,

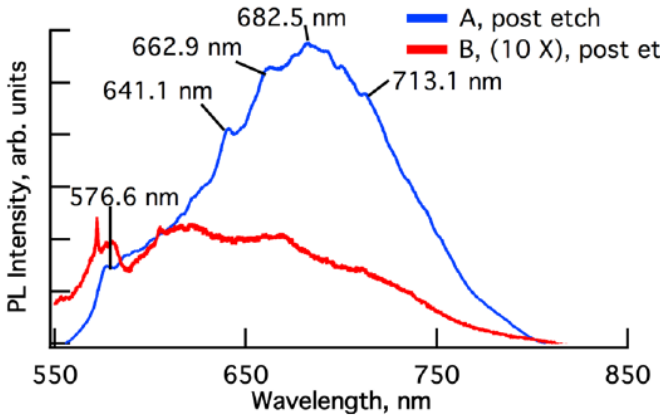

Figure 2.3.2: Luminescence from the thinned A (blue) and B (red) membrane samples. The thinned A sample exhibits strong, broad-band luminescence similar to that of bulk diamond with peaks at 576.6 nm and 641.1 nm, corresponding to NV°and NV^-, respectively. Phonon replica separated by $\sim$ 65 meV appears at 662.9, 682.5, and 713.1 nm. The luminescence of B (red) is significantly weaker and blue-shifted, still exhibiting a peak at about 576 nm (NV°) but no NV^- peak. The spectra were offset for clarity.

shown in Figure 2.3.3(c). Sample B exhibits a two-peak Raman fit only until 800 nm of material remains, as seen in Figure 2.3.3(d). The HWN peak (closest to the signature of bulk diamond) is absent in the 400 nm thick membrane B, and the 200 nm thick membrane B demonstrates a single Raman peak at 1317 ± 2 cm^{-1} with a 27 ± 4 cm^{-1} FWHM, shown in Figure 2.3.3(c). With further thinning of sample B to below 100 nm, the 1317 cm^{-1} Raman line disappeared, and the Raman spectrum is dominated by two broad bands at 1336.4 and 1589 cm^{-1}, corresponding to the D-and G-bands, respectively, peaks characteristic of graphite.

Thus, the changes in Raman signatures of samples A and B provide a complementary profile of the effective range of damage in the diamond membranes: Fig-

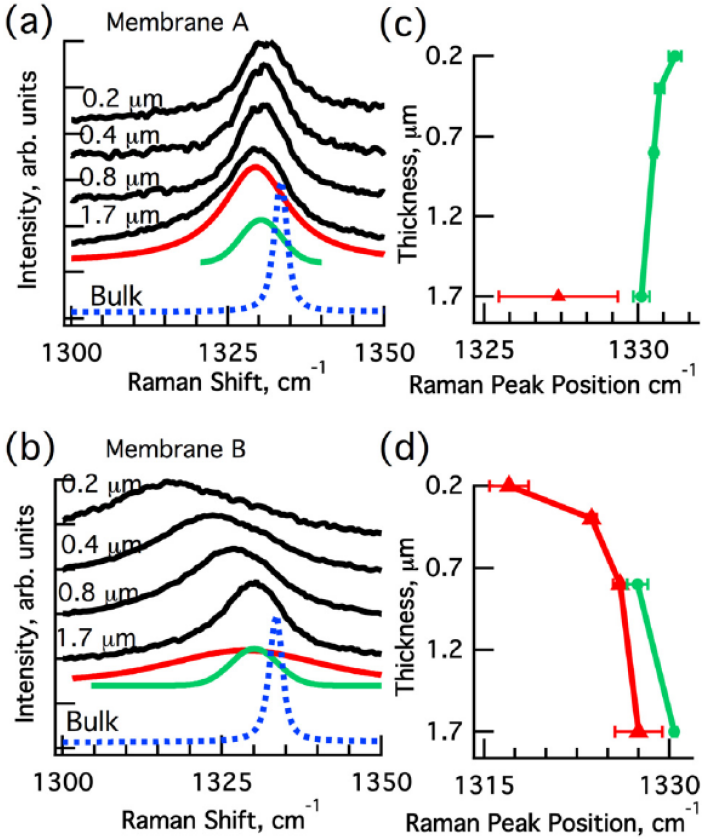

Figure 2.3.3: The shift in the first-order diamond Raman line as the A (a) and B (b) membranes are thinned. The Raman signal of the bulk diamond sample (dotted blue) is shown for comparison. The membrane thickness is indicated above each curve. The Raman signal was deconvoluted into two Voigt peaks, (red and green curves), shown for the 1.7 μm membrane. The change in the center frequency is shown for each Voigt peak for membranes A (c) and B (d). As A is thinned (c), the LWN component rapidly disappears, and the HWN component shifts towards the bulk Raman signal. Analogously, as B is thinned (d) the HWN component disappears after the removal of about 1.2 μm of material, and the center frequencies shift significantly towards LWN.

ure 2.3.3(a) for sample A suggests that removal of the material within one micron of the peak of the implant results in greatly improved material whose Raman signature essentially does not change with further thinning. Figure 2.3.3(b) for sample B provides further detail on the damage profile. The disappearance of the HWN component in the 400–800 nm of material closest to the end of range, coupled with the significant shift and broadening of the Raman peak to LWN are indicative of the significant damage to this region of the membrane. Thus, in addition to having poor luminescence, the material closest to the end of ion range has significantly degraded Raman character, indicating the removal of this portion of the membrane is important to fabricating a high-quality diamond photonic structure.

2.4 Observation of whispering gallery modes from single-crystal diamond microdisks

In this section, we describe the first observations of WGMs from microdisk cavities made from the lifted-off membrane obtained using ion-slicing methods. The diamond membrane is flipped and thinned using ICP-RIE to remove the more damaged layer. By placing the diamond membranes on a low refractive index dielectric material (SiO_2, $n \sim 1.46$), optical confinement can still be maintained.

The lifted-off diamond membrane was transferred to a 1 μm SiO_2-on-Si substrate using a droplet of water with a pipette tip. The surface near the heavily damaged layer were facing up. The more heavily damaged layer was removed using an argon chlorine ($Ar\text{-}Cl_2$) based ICP-RIE followed by an O_2-ICP-RIE. The membrane was thinned down to $\sim$ 300 nm. A 300 nm thick SiO2 hard mask was de-

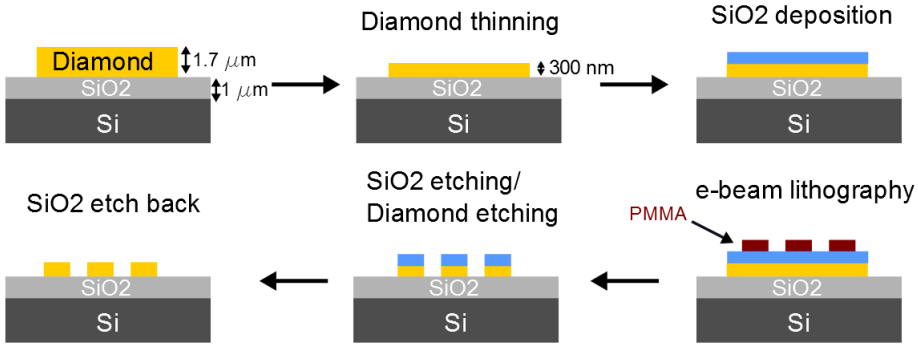

Figure 2.4.1: The diamond membranes were placed on a 1μm SiO_2-on-Si substrate. The unwanted heavily damaged regions was etched away using a combination of Ar/Cl_2 based ICP-RIE and O_2-ICP-RIE process. A 300 nm thick SiO_2 hard mask were deposited using PECVD. The microdisk patterns were defined using e-beam lithography followed by a fluorine based ICP-RIE to first etch the SiO_2 hard mask, and a O_2-ICP-RIE to etch the diamond layer. The remaining SiO_2 hard mask layer was removed by an etch back using fluorine based ICP-RIE. The low refractive index SiO_2 ($n \sim 1.46$) underneath layer provided sufficient optical confinement.

posited using PECVD. The pattern were defined using 100 KeV electron-beam lithography (Elionix 7000), with poly-methyl methacrylate (PMMA) as the e-beam resist. The patterns are transferred by first etching the SiO_2 hard mask using fluorine based ICP-RIE process and then a O_2-ICP-RIE process to etch into the diamond. The hard mask was removed by an etch back procedure using the fluorine based ICP-RIE (Fig2.4.1). The resulting device was a diamond micro-disk on top of a lower index ($n \sim 1.46$) 1 μm SiO_2-on-Si substrate, shown in Figure 2.4.2(a).

Figure 2.4.2(a) shows a 2 μm diameter diamond disk-on-SiO_2 fabricated from the lifted-off diamond membranes. The Raman peak from the diamond membrane after thinning was fitted with a single Voigt profile. The Raman peak was

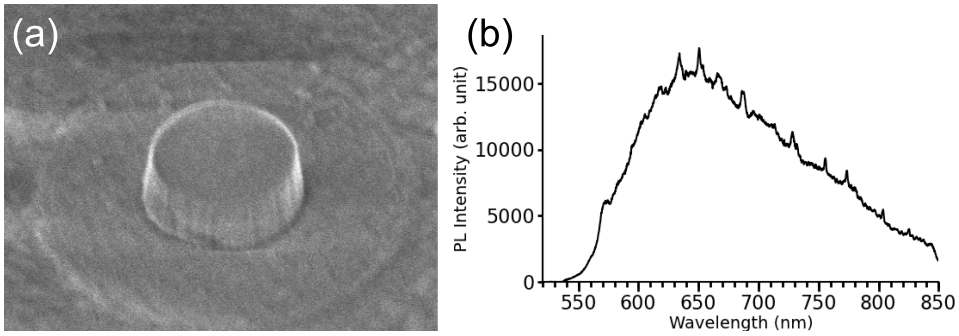

Figure 2.4.2: (a) The SEM image of 2μm diameter microdisk made from lifted-off membranes. The diamond microdisk cavities on top of a 1μm SiO2-on-Si substrate. (b) WGMs were observed from the microdisk cavities, the Q $\sim$ 500.

centered at 1330.5 cm^{-1} with a $\sim$ 8.2 cm^{-1} FWHM which indicated the device layer was the less damaged part of the membranes. WGMs were observed from microdisk cavities made from the lifted-off membranes using μ-PL measurement with a confocal microscope and 532 nm laser excitation (Figure 2.4.2(b)). The WGM exhibited Q as high as $\sim$ 500, where the disk material was the less damaged region from the diamond membranes. The Q of the 2μm diameter diamond disk-on-SiO_2 were simulated using finite difference time domain (FDTD) simulation using a commercial software (Lumerical Inc.). Q $\sim$ 250,000 was deduced from WGMs with transverse electric polarization and zeroth order in the radial direction which was much higher compared to the experimental value. We believe the main limitation of Q is the optical losses to defects in the membrane, resulting from residual damage from the ion implantation process. Such residual damage is evident from the Raman characterization described in the previous section.

2.5 Summary

Single crystal diamond membranes with 1.7 μm thickness were fabricated using the ion slicing method. Strongly luminescent diamond membranes with 200 nm thickness were fabricated by removing the damaged area of a lifted-off single-crystal diamond membranes. The correlation between luminescence in the membrane and the Raman shift clearly emphasize the importance of further processing of the lifted-off diamond membranes to remove the heavily damaged material. Microdisk cavities were made out of the less damaged material, and showed Q as high as $\sim$ 500. The main limitation of the Q factor is believed to be due to the residual damage in the membranes. Therefore, diamond cavities with high Q are expected by improving the material properties of the lifted-off diamond membranes.

3

Homo-epitaxial diamond overgrowth on diamond membranes

3.1 Introduction

In the previous chapter, we have demonstrated a technique to lift off single-crystal diamond membranes from bulk diamond using an ion-slicing method. Microdisk

cavities were fabricated from lifted-off diamond membranes. However, the quality of the membranes was degraded by the ion damage during processing and the Q of the microdisk was limited to $\sim$ 500. In order to fabricate diamond membranes that are useful for photonics applications, the material quality needs further improvement. In this chapter, we describe the formation of high quality diamond membranes by performing a homo-epitaxial overgrowth using the lifted-off diamond membranes as the template layer. The overgrown layer showed improved material quality with a narrow Raman linewidth ~ 2.5 cm^{-1}. In contrast to the template material, nitrogen vacancy (NV) centers were observed using microphotoluminescence (μ-PL) measurements and electron spin resonance (ESR) techniques. Ensemble NV centers in the overgrown layer showed good spin coherence properties comparable to natural NVs in type Ib diamond [72] and shallow implanted NVs in a high purity bulk diamond [15, 73]. Different color centers were incorporated in the overgrown layer during growth by putting the template membranes on different substrates (e.g. silicon, bulk diamond). Silicon vacancy (SiV) centers were observed in the overgrown layer. Microdisk cavities made from the overgrown layer showed higher Q ($\sim$ 3,000). Optical coupling of the SiV centers with a whispering gallery mode (WGM) with Q $\sim$ 2,500 was observed. By combining the ion-slicing technique with diamond overgrowth method, high quality diamond membranes were fabricated for photonics applications.

3.2 Diamond overgrowth

There has been much progress on diamond growth using the chemical vapor deposition (CVD) method [74]. The growth process is a kinetic process, where carbons are deposited onto the diamond surface with the supply of methane plasma and the atomic hydrogen preferentially removing the sp^2 bond carbon on the surface which sp^3 bond carbon were deposited on surface. Homo-epitaxial overgrowth on implanted diamond was demonstrated in the 1990's. Diamond films were grown on ion implanted bulk diamond which were subsequently lifted-off. The overgrown layers showed a narrow Raman line $\sim$ 2.5 cm^{-1} [75]. Millimeter-size diamond membranes were fabricated using such approaches [61]. The substrate can be re-used for many times also make this approach economical [67].

However, all the earlier reported diamond membranes reported had overgrown layer thicknesses from 10 μm to 70 μm which are too thick for photonics applications. In this chapter, we describe our approach to fabricate high quality thin diamond membranes (200 nm - 300 nm) for photonics application using homo-epitaxial growth on lifted-off diamond membranes.

The original single crystal diamond membranes were first cleaned using a mixed (1:1:1 sulfuric–perchloric–nitric) acid and put into a Seki Technotron AX5010-INT PECVD reactor. The chamber was evacuated below 0.1 mTorr and flushed with H_2 gas. After the plasma ignition (only hydrogen ambient), it took approximately 8 minutes for the temperature and the pressure to stabilize, at which time the methane was introduced. The growth conditions were: microwave power 950

W, pressure 60 Torr, 400 SCCM of 1:99 CH_4 (99.999 %)/H_2(99.999%) for 5 minutes. No external heating source was used and the temperature was $\sim 850^{\circ}$C as read by a pyrometer. We note that our growth conditions are not typical of those used for homo-epitaxial, single-crystal diamond growth, which often requires higher microwave power densities ($\sim$ 2–4 kW) and higher pressure ($\sim$ 150–250 Torr)[74, 76].

The structural properties of the overgrown membrane were characterized using scanning electron microscopy. Figures 3.2.1(b),(c) show the top view and the cross sectional SEM images of the original membrane, 1.7μm in thickness. Figures 3.2.1(d),(e) illustrate the overgrown material after 5 minutes of growth. The single crystal material, with a top (100) facet, was clearly observed on top of the original membrane. No indications of polycrystalline material, grain boundaries or surface defects (e.g., hillocks) were observed. The pits in the regrown layer were transferred from the original membrane, which was pitted. In principle, this could be avoided through the use of smooth, dislocation-free, single crystal diamond as a starting material. Importantly, the undamaged regions of the overgrown material were very smooth. Atomic force microscope (AFM) scans revealed that the root mean square (RMS) surface roughness was only 4 nm (Figure 3.2.1(d)). In comparison, the RMS surface roughness of a typical commercially available CVD single crystal diamond (Element Six, Inc) was on the order of 2–3 nm.

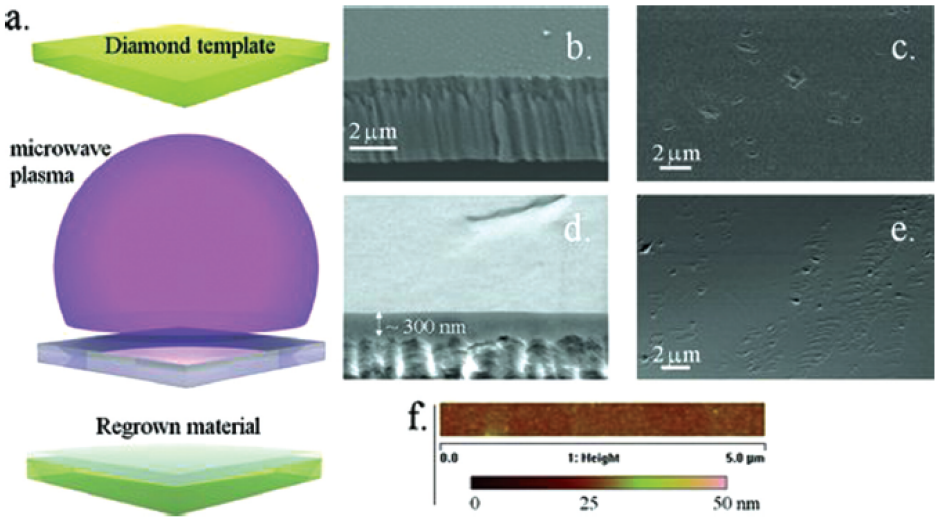

Figure 3.2.1: (a) Schematic illustration of the regrowth process of the diamond membrane using a PECVD reactor. (b) SEM side view and (c) top view of the original diamond membrane before the regrowth. (d) SEM side view and (e) top view showing a $\sim$ 300 nm overgrowth of a single crystal diamond. The pits observed on the surface were transferred from the original membrane. (f) AFM scan of a 5 μm strip demonstrated the smoothness of the top membrane surface. The surface roughness was measured to be 4 nm.

3.3 Optical properties of the re-grown films

3.3.1 Improved Raman characteristics

Raman spectroscopy provides information on the crystal quality of the diamond membranes. The material quality of the overgrown layer was characterized using optical methods such as Raman spectroscopy and μ-PL measurements. The best diamond template showed a Raman peak at 1331 cm^{-1} with a full width at half maximum (FWHM) of 9.9 cm^{-1} (after removing the most damaged region but without annealing or overgrowth treatment)[18]. However, it was still broader compared to the Raman peak measured from bulk diamond which was centered at 1333.5 cm^{-1} with a FWHM 2.3 cm^{-1}. After a diamond overgrowth on the less damaged side of the diamond template, the composite overgrown membrane-plus-template was flipped and thinned using O_2-ICP-RIE to remove the heavily damaged region from the template material. The Raman line of the composite overgrown membrane-plus-template gave a peak value of 1332 cm^{-1} with a FWHM of 6.6 cm^{-1}. These values were a convolution of the Raman peak from the overgrown material with that of the diamond template, and accounted for the best fit to two Voigt peaks, shown in Figure 3.3.1(a). The broader peak at lower wave number corresponds to the Raman peak from the template material (green curve in Fig. 3.3.1(a), centered at 1329.6 cm^{-1} with a FWHM of 8.1 cm^{-1}) and the narrower peak corresponds to the Raman peak from the overgrown material (blue curve in Fig. 3.3.1(a), centered at 1332.9 cm^{-1} with a FWHM of 4.3 cm^{-1}). After further thinning, a narrower Raman line was observed from the overgrown mem-

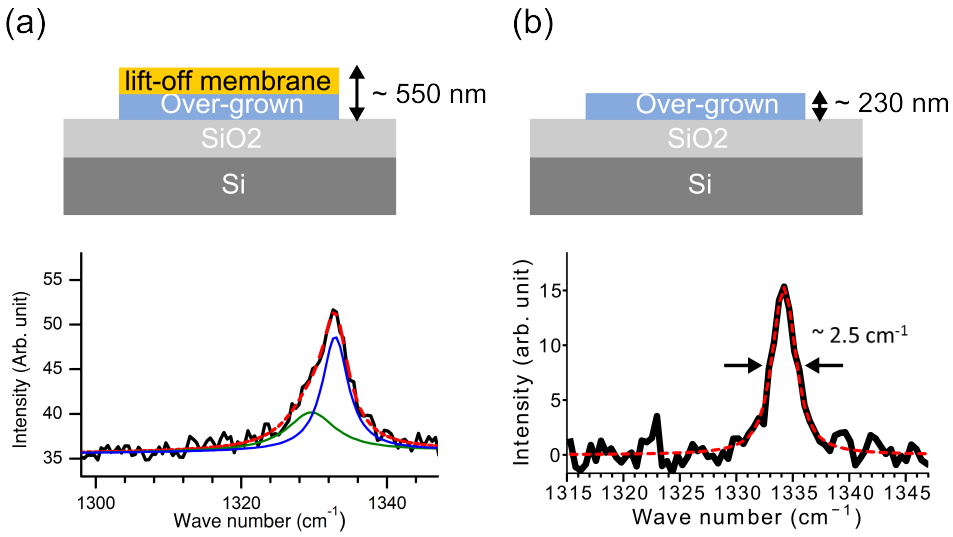

Figure 3.3.1: Improved Raman signature was observed from the overgrown membrane. (a) The Raman line of a composite overgrown membrane-plus-template is best fit to two peaks, one correspond to the template material (green curve), the other correspond to the overgrown membrane (blue curve). (b) The Raman character of the overgrown membrane was revealed by measuring the Raman line from the overgrown membrane only (after removing the template material completely with ICP-RIE etching). The Raman line is best fit to a single peak and the linewidth is ~ 2.5 cm^{-1}, which is narrower compared to the template material (~ 9.9 cm^{-1}).

brane centered at 1334.2 cm^{-1} with a FWHM of 2.5 cm^{-1} which was very close to the Raman line measured from bulk diamond.

To further gauge the influence of the template quality on the properties of the overgrown diamond, material was overgrown on the template material where the *less* damaged material was removed by ICP-RIE process (Figure 3.3.2(b)). Even with a heavily damaged template material, the epitaxially grown material exhibited superior Raman characteristics with linewidth of ~ 3 cm^{-1}, approaching the quality of a bulk single crystal diamond, despite the shifted and much broader Raman

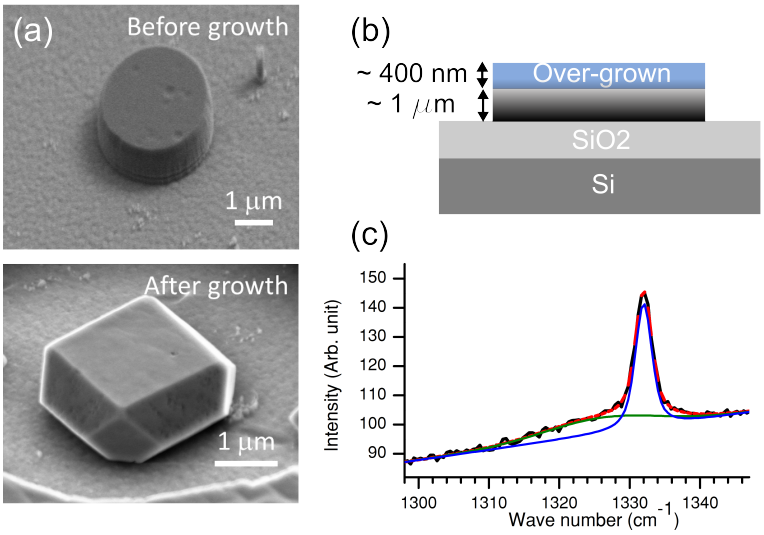

Figure 3.3.2: The Raman linewidth of the overgrown film was narrower compared to the Raman line of the ion damaged membranes. (a) SEM cross section of the diamond membranes before growth and after growth. (b) The overgrown layer was on a heavily damaged diamond template where the less damaged layer was removed using ICP-RIE. (c) The Raman line of the composite overgrown membrane-plus-heavily damaged template was best fit by two peaks. A narrow Raman line from the overgrown membrane was measured (blue curve, centered at 1332.0 cm^{-1} with a FWHM of 2.8 cm^{-1}) despite a shifted and broader Raman line from the template membrane (green curve, centered at 1325.6 cm^{-1} with a FWHM of 19.4 cm^{-1}).

signature of the template, as seen in the green curve of Figure 3.3.2(c). This is convincing evidence that the overgrown diamond film has much improved structural properties over its highly-damaged, highly-strained diamond template. This is contrary to conventional epitaxial growth of other semiconductors (e.g., GaAs) where the defects in the template are manifested in the properties of the overgrown material and often reduces its quality[77]. However, strain fields do exist in our grown material, as is suggested by the double dip in the optically detected magnetic resonance (ODMR) measurements (Figure 3.3.3(b)).

3.3.2 Nitrogen vacancy centers in overgrown material

In the previous chapter, strong NV-like fluorescence was observed from the less damaged lifted-off membranes, however, no ESR signal of NV centers was observed [18]. In this study, the overgrown membranes were characterized using μ-PL measurement under 532 nm excitation at room temperature and by ESR measurements. Bright fluorescence and the spectral signature of NV centers was observed on one of the overgrown samples where the template membrane was etched away using an Ar-Cl_2 based ICP-RIE followed by a O_2-ICP-RIE shown in Figure 3.3.3(a). The existence of NV centers in the overgrown membrane was confirmed by the observation of the ESR dips as shown in Figure 3.3.3(b). The diamond sample was measured using a confocal microscopy setup with a 100 $\times$ objective with a 532 nm laser for photoexcitation. A microwave magnetic field was coupled to the NV centers through a metal wire loop connected to power amplifier and the PL from NV centers was collected through the same objective with no ap-

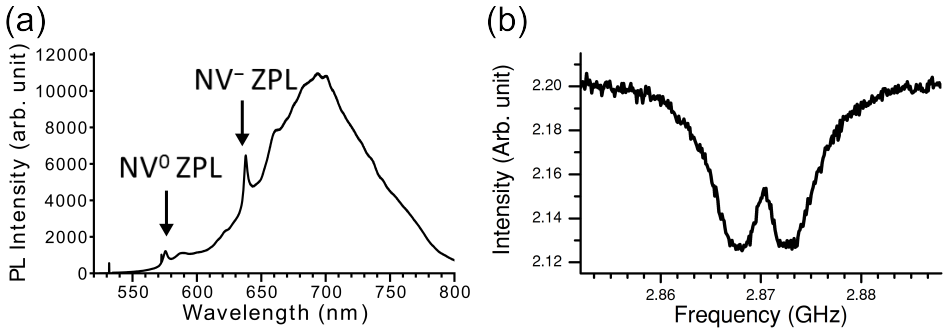

Figure 3.3.3: NV centers were incorporated into the overgrown membrane during growth. (a) PL spectrum of the overgrown membranes showed bright fluorescence, zero phonon line of NV° and NV^- was observed. (b) ESR signal of NV centers was observed in the overgrown membranes, confirmed presence of NV centers in the overgrown membranes. There were no external magnetic field applied during the measurement. The peak splitting of the ESR signal suggests existence of strain in the overgrown membranes. The ESR measurement was performed by Bob Buckley and Christopher Yale in David Awschalom's lab at UCSB.

plied magnetic field. The two ESR dips observed are thought to be due to strain in the membranes. We note that there was no nitrogen incorporated during the diamond growth; the nitrogen source was due to residual gas in the chamber. The observation of the ESR dips from the NV centers in the overgrown membranes motivated further investigations of the spin coherence properties of NV centers in diamond. The spin coherence measurements were made in the lab of Professor David Awschalom at UCSB, with the help of Bob Buckley and Christopher Yale.

The spin coherence time determines the number of operations can be performed on a quantum bits before the information is lost. The ground state spins were first initialized using a 532 nm laser pulse of 5ms. Microwave magnetic fields were then applied using an arbitrary waveform generator for spin manipulation. The sample

PL was measured by an APD which was gated in time for time-domain spin coherence measurements. In figure 3.3.4, after a laser pulse that initialized the spin state, a single microwave magnetic field pulse whose frequency is resonant with the NV center's S_Z-S_X transition. The microwave "π" pulse flips the NV centers electronic spin state from the S_Z to S_X. The ensemble spin state is then measured with a second 532 nm "readout " laser pulse via PL intensity. The measurement was performed as a function of delay time (τ_1) between the initialization and readout 532 nm laser pulses. To normalize the PL and determine the spin contrast between S_Z and S_X, the resulting PL was subtracted from a similar sequence without the spin-flipping microwave π pulse. The resulting subtracted data is plotted in Figure 3.3.4 as a function of time. Fitting to an exponential decay reveals a spin-lattice relaxation time of T_1 = 5 ms for the NV center ensemble.

The transverse homogeneous spin coherence was measured with Hahn-echo sequences. The spin was first initialized into S_Z state with an initialization pulse of 3 μs. Then, a Hahn echo sequence was applied using microwave field pulses resonant with S_Z-S_X NV center spin transition. The Hahn echo began with a $\pi/2$ microwave pulse which rotated the spins onto the equator of the Bloch sphere. The pulse was followed by a π pulse after a time $\tau_2/2$. The final $\pi/2$ pulse, a time $\tau_2/2$ after the π pulse, flipped the spins back to the poles of the Bloch sphere for spin readout. Finally, the ensemble spin state was read out via PL using a 532 nm "readout" laser pulse. The free precession time, τ_2, was varied. To compensate for pulse errors, the center π pulse was 90° out of phase from the $\pi/2$ pulses. The spin contrast is plotted in plotted in Figure 3.3.5 as the difference in PL intensity

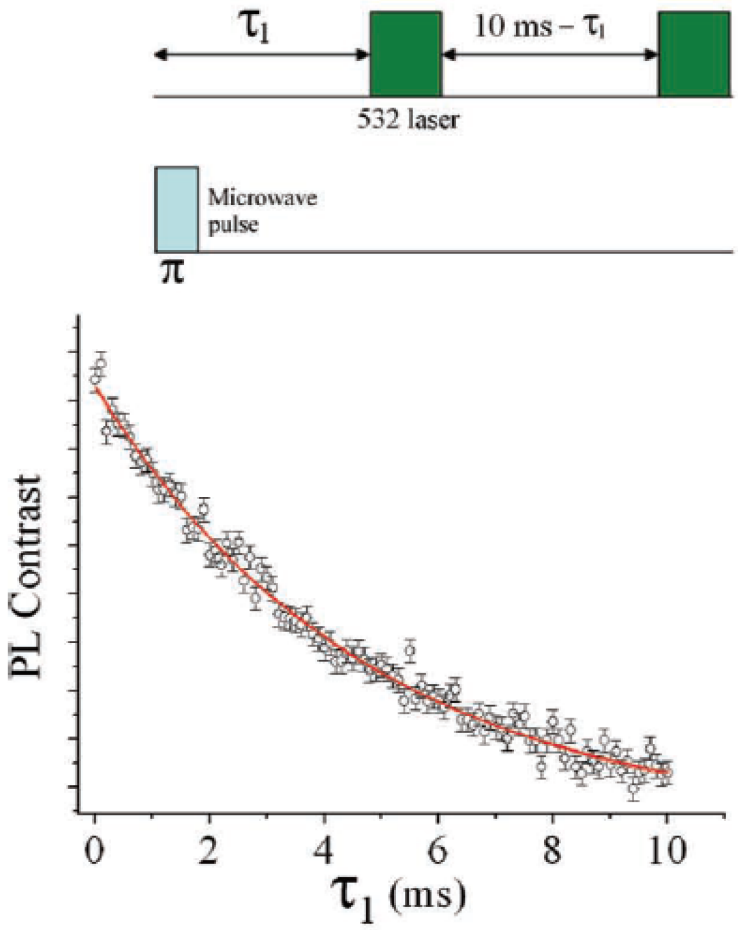

Figure 3.3.4: Spin lattice relaxation time, yielding $T_1 \sim 5$ ms. The red curve is a single exponential fit of the data. The red curve is a single exponential fit of the data. The sequences applied to measure the spin properties are schematically depicted. The data are recorded at room temperature with no applied magnetic field. The Spin coherence measurement was performed by Bob B. Buckley and Christopher Yale in David Awschalom's lab at UCSB.

between flipping and not flipping the sign of the final $\pi/2$ pulse relative to the initial $\pi/2$ pulse. Fitting this subtracted data to a single exponential decay determined T_2 = 3.5 μs.

The transverse inhomogeneous spin coherence time was determined with a Ramsey timing sequence (Figure 3.3.6). The spin was initialized into S_Z state with a laser pulse of 3 μs. The Ramsey sequence consists of two $\pi/2$ pulses separated by a time τ_2^*, which was varied. Like the Hahn echo sequence, the spin contrast is the difference in PL intensity between whether the sign of the last $\pi/2$ pulse is flipped or not, relative to the initial $\pi/2$ pulses. Ramsey sequences were typically performed with a detuned microwave frequency, and in this sequence, the microwave were detuned by 25 MHz from the S_X resonance in order to induce oscillations in the data. We observed beating of four frequencies (two frequencies per spin resonance peak), which suggested a small magnetic field or asymmetric strain may play a role in splitting the S_X and S_Y spin sub-levels of NV centers. The data, plotted in Figure 3.3.6, was fit to four beating frequencies with a single exponential decay envelope revealed T_2^* = 158 ns for this ensemble of NV centers.

It should be noted that transverse spin coherence is sensitive to the surrounding spin bath, originating from the presence of other electron and nuclear spins as well as magnetic fluctuations on the surface. The measured values of T_2 and T_2^* for the overgrown material are comparable with both natural NVs in type Ib diamond[72] and shallow implanted NVs in a high purity bulk diamond[15, 73] (T_2 1-20 μs) and are higher than typical coherence times found in nanodiamonds ($T_2 \sim 1$ μs)

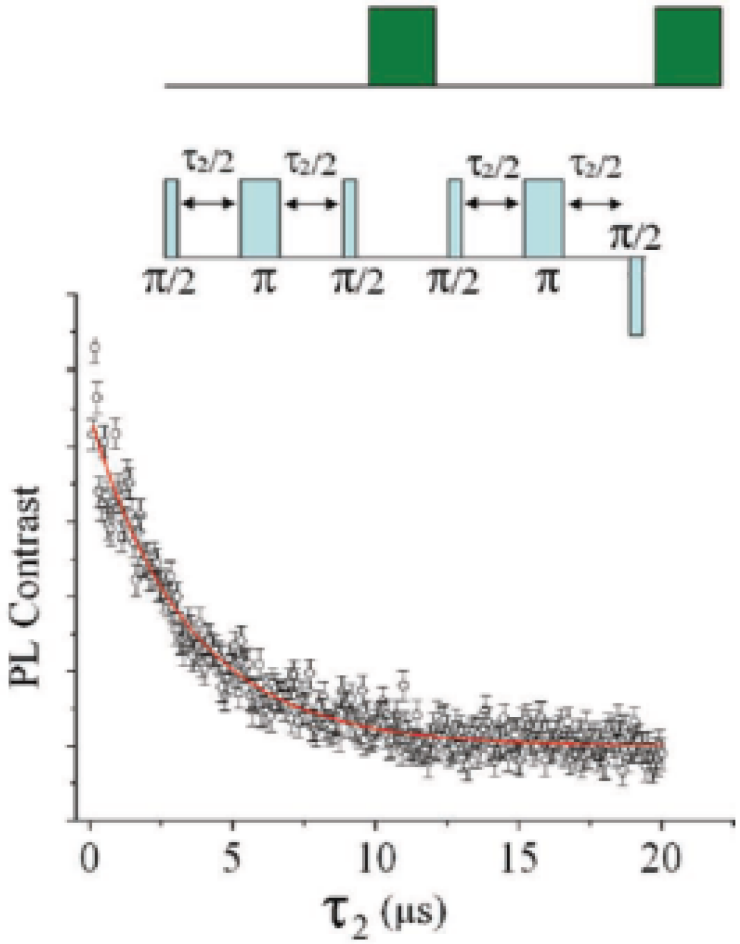

Figure 3.3.5: Hahn-echo sequence of the transverse homogeneous spin coherence time resulting with a $T_2 \sim 3.5$ μs. The red curve is a single exponential fit of the data. The sequences applied to measure the spin properties are schematically depicted. The data are recorded at room temperature with no applied magnetic field. The Spin coherence measurement was performed by Bob Buckley and Christopher Yale in David Awschalom's lab at UCSB.

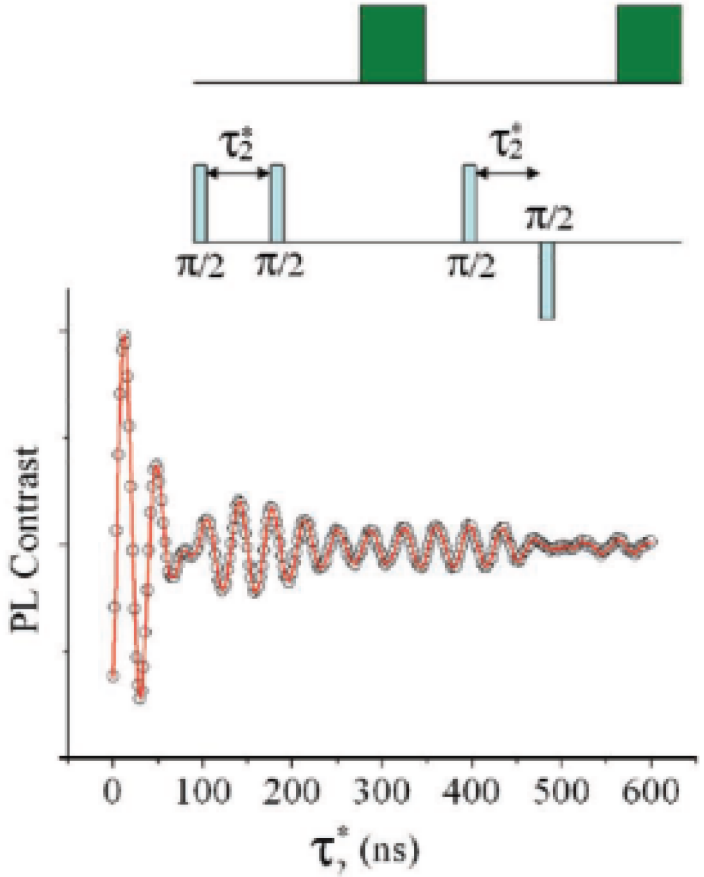

Figure 3.3.6: Ramsey sequence to determine transverse inhomogeneous spin coherence precession decay time, yielding $T_2^* = 158$ ns. Error bars are smaller than data markers. The sequences applied to measure the spin properties are schematically depicted. All the data are recorded at room temperature with no applied magnetic field. The Spin coherence measurement was performed by Bob Buckley and Christopher Yale in David Awschalom's lab at UCSB.

[78]. Nevertheless, T_2 = 3.5 μs is still shorter than for the isotopically pure single crystal diamond ($T_2 \sim$ 1 ms) [3]. Remarkably, good spin behavior exists in the overgrown material despite the fact that the original template did not show any ODMR signal and the overgrown membrane is only a few hundred nanometers thick. The spin properties of the overgrown membrane further confirm the good quality of the thin, single crystal diamond membrane and indicate promise for applications in nano-magnetometry and QIP.

The spin properties of the overgrown diamond membranes can be significantly improved by growing material in a purer environment, resulting in fewer paramagnetic defects such as substitutional nitrogen. Additionally, growing with ^{12}C isotopically purified methane has the promise to achieve millisecond T_2 coherence times, as the nuclear spin of ^{13}C can significantly reduce the NV spin coherence[3]. Furthermore, additional experimental steps such as high temperature annealing[73] may also improve the coherence times of NV centers in the grown material.

3.4 Whispering gallery mode based cavities from overgrown membranes

Microdisk cavities fabricated from the template membranes showed limited Q ($\sim$ 500). The limitation of Q was due to the ion damage during processing. By fabricating optical cavities from overgrown material, we show that with the improved material quality from the overgrown membranes, the Q of the cavities also improved.

Microdisk cavities were made from overgrown membranes to compare with

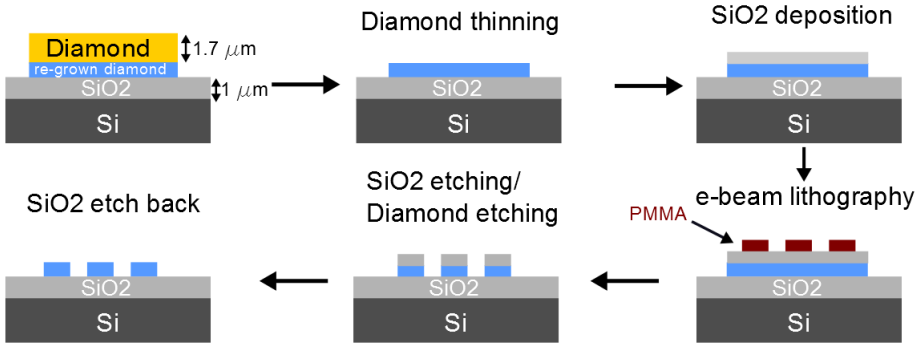

Figure 3.4.1: Microdisk and ring cavities were made out of overgrown membranes. The diamond membranes were placed on a 1μm SiO2-on-Silicon substrate. After the growth, the composite overgrown membrane-plus-template was flipped and thinned using an Ar/Cl2 based ICP-RIE followed by oxygen ICP-RIE. SiO2 is deposited on the membranes as a hard mask using PECVD. Electron beam lithography is used to pattern with PMMA as resist. The patterns were transferred by etching the SiO2 hard mask and diamond using ICP-RIE.

devices made from template membranes. The overgrown membrane were first flipped and thinned using an ICP-RIE process. An 80 nm thick silicon dioxide mask was deposited by PECVD. The ring/disk cavities were patterned using a 100 KeV electron beam lithography (Elionix) with poly (methyl methacrylate) (PMMA) as the resist. The patterns were then transferred by a fluorine based ICP-RIE step to etch into the silicon dioxide hard mask, followed by a O_2-ICP-RIE step to transfer the pattern to the diamond membrane (Figure 3.4.1).

A SEM image of a microdisk cavity made from the overgrown diamond is shown in Figure 3.4.2 (a). The diameter of the microdisk was 3 μm with thickness of $\sim$ 170 nm. The WGMs were observed using a μ-PL measurement with a confocal microscope (LabRAM ARAMIS, Horiba Jobin-Yvon) and 532 nm laser excitation

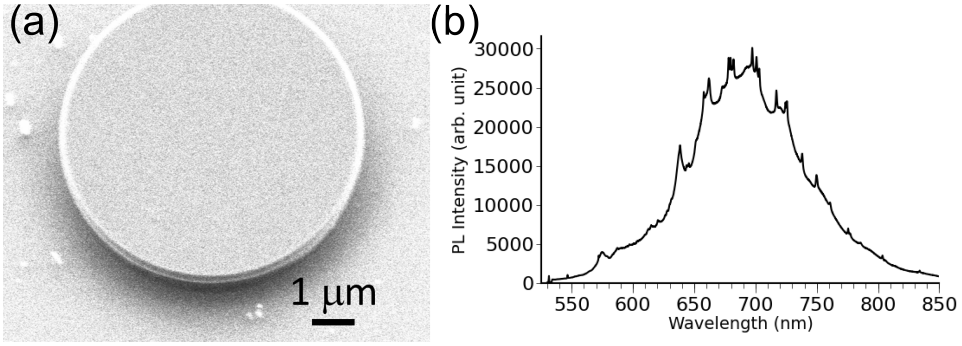

Figure 3.4.2: Microdisk cavities fabricated from overgrown material show Q $\sim$ 3,000. (a) SEM viewgraph of a diamond microdisk resonator made from overgrown membranes (b) WGMs were observed from the microdisk cavity using μ-PL measurement. The WGMs were decorated by the NV fluorescence from the membrane. The device shown in the SEM is a similar device.

(Figure 3.4.2(b)). The WGMs were decorated by NV fluorescence in the cavity medium that were excited by the 532 nm laser. The excitation and signal collection went through the same objective with numerical aperture (NA) = 0.9 and magnification 100$\times$ which results in spatial resolution $\sim$ 1 μm. WGMs with Q as high as 3,000 were observed from disk made out of overgrown membranes which was better compared to the disk made from template membranes. This result showed that with improved material quality, the device performance also improved.

Ring cavities with outer diameter 3.5 μm and inner diameter 2.3 μm and thickness of $\sim$ 170 nm were fabricated from the overgrown membrane shown in Figure 3.4.3(a). WGMs with better signal to noise contrast was observed compared to the microdisk cavities as shown in Figure 3.4.3(b).

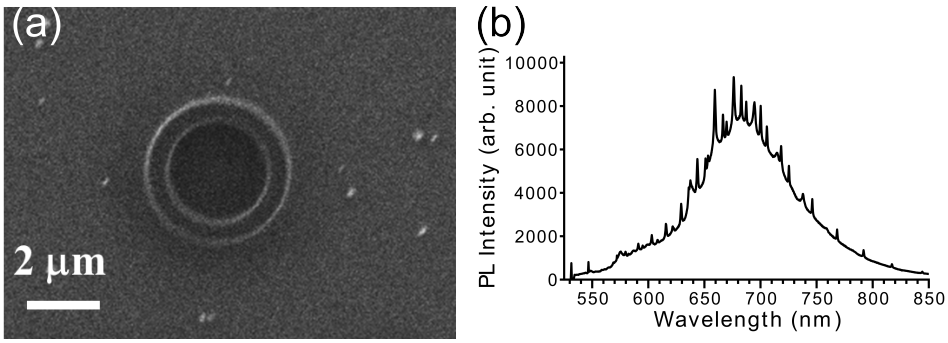

Figure 3.4.3: Ring resonators fabricated from overgrown material show Q $\sim$ 3,000. (a) SEM viewgraph of a diamond ring resonator made from overgrown membranes (b) WGM were observed from the ring resonator using μ-PL measurement. The device shown in the SEM is a similar device.

3.5 Optical coupling to silicon vacancy centers

3.5.1 Silicon vacancy centers in overgrown membranes

Besides NV centers in diamond, there are also various different color centers in diamond which have unique physical properties. Intense research efforts on individual color centers in diamond over the past decade have yielded significant insight into the photo-physics of defects in diamond. In particular, there is a growing interest in utilizing color centers that exhibit a narrow luminescence band, short excited state lifetime, and single photon emission at room temperature[25, 26]. Such defects are extremely attractive photon sources for quantum key distribution or optical quantum computation [79].

Different color defects can also be incorporated during the overgrowth process by controlling the template on various substrates, e.g., silicon or other bulk diamond. We have demonstrated this by incorporating a different color center, SiV

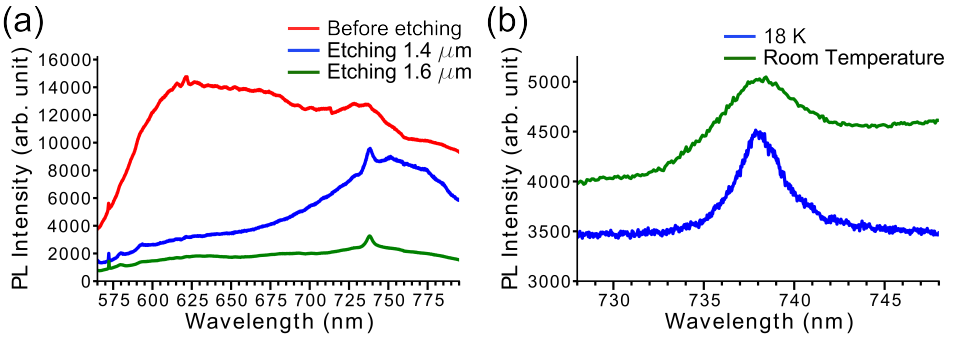

Figure 3.5.1: (a) Room temperature PL curves recorded from the membrane immediately after regrowth (blue curve), after a subsequent removal of $\sim$ 1.4 μm of the original template (green curve) and a final thinning to 300 nm thick membrane (100nm:200nm original template:overgrown layer). A pronounced ZPL from the SiV centers was observed as the original template is removed. The FWHM of the ZPL is $\sim$ 6 nm. (b) Low temperature PL measurement recorded from the membrane after removal of $\sim$ 1.4 mm of the original membrane. The FWHM of the ZPL of SiV centers at 9 K is $\sim$ 3 nm.

centers, into the overgrown membranes. The SiV centers consist of a silicon atom in the split-vacancy configuration [80]. The PL of the membranes is presented in Figure3.5.1, where the ZPL (at 738 nm) of SiV centers was observed. We believe that during the growth the plasma slightly etches the substrates, whose elements are subsequently incorporated into the growing diamond lattice[81]. Therefore, incorporating different color centers in diamond membranes using the overgrowth method opens opportunities to integrate different single photon source (NV, SiV, Cr) in diamond devices.

Figure 3.5.1(a) shows the room temperature PL spectra of the diamond membrane before thinning (blue curve) and after the removal of $\sim$ 1.4 μm (green curve) and $\sim$ 1.6 μm (red curve) of the original diamond template. Broadband luminescence obscured the luminescence of SiV centers before the membrane was thinned

(Figure 3.5.1(a) blue curve). The broadband luminescence was further reduced through the removal of the original diamond template using ICP-RIE (Figure 3.5.1(a) green and red curves). A pronounced ZPL at 738 nm attributed to the SiV was clearly seen after most of the original template was etched away. The FWHM of the ZPL was measured to be $\sim$ 6 nm at room temperature. At low temperature (18 K) the FWHM was reduced to $\sim$ 3 nm (Figure 3.5.1(b)), however, the fine structure of the defect (Fig. 1(b)) was not resolved [81, 82] due to a high concentration of the emitters and their inhomogeneous broadening due to the strain fields.

Using the overgrowth technique, different color centers could be incorporated in the diamond membranes. The overgrown membranes showed narrower Raman linewidth compared to the template layer, which suggested improved material quality from the overgrown membranes. These results opened up opportunities to couple different color centers in diamond photonic devices made from overgrown membranes.

3.5.2 Optical coupling

With the improved device performance, and the ability to incorporate different color centers in the overgrown membranes,we explored the possibility to couple different emitters in diamond to the cavity modes.

Microdisk cavities with a diameter of 2.5 μm and a thickness of 500 nm were fabricated from a composite overgrown membrane-plus-template. The fluorescence of SiV centers was observed from the overgrown membrane. WGMs were

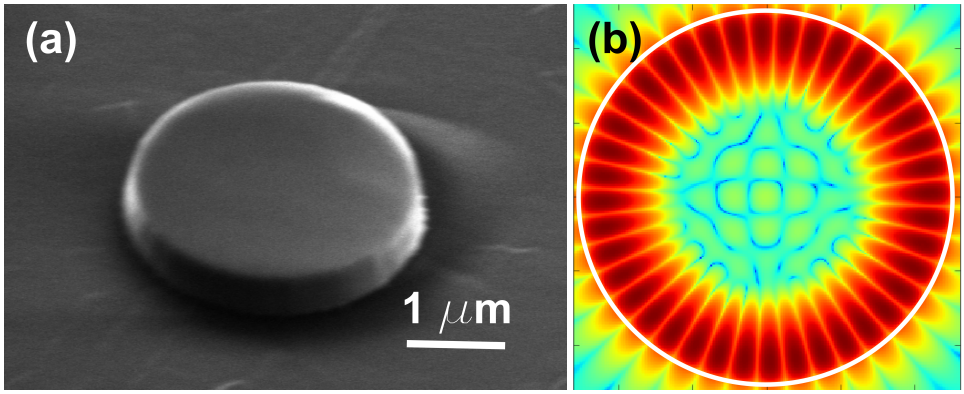

Figure 3.5.2: (a) SEM image of 2.5 μm diameter disk fabricated from single-crystal diamond. (b) FDTD simulation of the field intensity (H_Z) profilein log scale for the TE mode with zeroth order in radial direction ($TE_o^{m=20}$). The red color indicates higher field intensity, and the white circle indicates the periphery of the microdisk.

observed using μ-PL measurement (Figure 3.5.3(a)). By comparing the free spectral range of the WGMs to the finite-difference time domain (FDTD) simulations (Lumerical Solutions, Inc.), the polarization and the order (both radial and azimuthal direction) of the WGMs were identified (Figure 3.5.3(b)). Quality factors, Q, of these modes were determined to be $\sim$ 2200. The modal volume of the zeroth order WGM in the radial direction with transverse electric (TE) polarization was $\sim$ 0.273 μm^3 (9.6 $(\lambda/n)^3$) calculated using FDTD simulations.

A high resolution spectrum of the TE mode centered at 736.5 nm is shown in Fig. 3.5.4(a). The mode was found to be zeroth order in the radial direction ($TE_o^{m=20}$) with Q $\sim$ 2200 and overlaps spectrally with the SiV ZPL emission. To investigate the emitter-cavity system further, lifetime measurements were performed. A frequency-doubled pulsed Ti:Sapphire laser at 460 nm with a 76 MHz

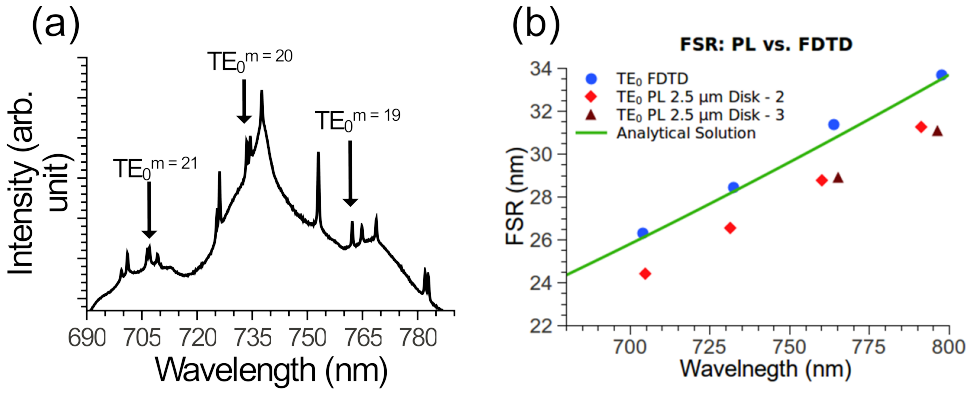

Figure 3.5.3: (a). Room temperature PL spectrum recorded from the microdisk cavity with 20 mW laser excitation. The WGMs were observed. The zeroth order radial TE mode had a Q of $\sim$ 2200. (b). Assignment of the WGM was made by comparing the experimental measurement of the free spectral range (FSR) of the whispering gallery modes to FDTD simulation. The PL spectrum measured from a 2.5 μm diameter disk showed similar FSR to the simulation but the resonances were shifted slightly.

repetition rate and pulse width less than 70 femtoseconds was used to excite the SiV emitters. The 18K measurement was made with the sample in a cryostat (Janis) with excitation and signal collection passing through the same NA = 0.5 objective, with 100$\times$ magnification and 1 mW laser excitation power. The laser light was reflected by a dichroic mirror and the collected PL signal was filtered by a band pass filter (747 nm $\pm$ 17 nm) and directed onto an APD (Micro Photonic Devices, jitter time $\sim$ 50 ps). The spectral window includes both the enhanced part and non-enhanced luminescence from the SiV centers. The cavity mode linewidth is $\sim$ 0.336 nm and the linewidth of the SiV ZPL is $\sim$ 3 nm. Therefore, we approximated $\sim$ 10% of the SiV centers were coupled to the cavity modes, taking into account that the Debye-Waller factor is $\sim$ 80% as reported in the literature [5].The results of the lifetime measurements are shown in Fig. 3.5.4(b) and are best fit

with a bi-exponential decay. The lifetime of the SiV centers coupled to the microdisk was measured to be $\sim$ 1.48 $\pm$ 0.04 ns while the lifetime measured from the membrane outside of the disk is $\sim$ 1.83 $\pm$ 0.09 ns. The second part of the bi-exponential fit accounted for the fast decays which were measured to be 0.66 $\pm$ 0.02 ns from the membrane and 0.43 $\pm$ 0.01 ns from the cavity due to other defects in the membranes. The lifetime reduction was in reference to a diamond membrane having the same thickness and having undergone exactly the same fabrication process as the microdisk cavities. Hence, other reasons for lifetime reduction, e.g. non radiative channels or surface defects, if present, would be the same in both the membrane and the microdisk. Therefore, we believed that the only reason for the observed lifetime reduction was the modification of the density of states of the emitters due to coupling to the cavity modes. The Purcell enhancement based on lifetime modification was estimated to be $\sim$ 1.3. The reduced lifetime value could be regarded as an averaged lifetime of multiple different exponential decay curves, which represented different SiV centers in the disk coupled to the cavity mode. Additionally, an enhanced photon count rate from the APD was observed from the microdisk ($\sim$ 40,000 counts/s) compared to the diamond membrane ($\sim$ 3000 counts/s) under identical excitation conditions. The microdisk cavity could increase the far-field collection through geometrical effects that enhanced photon extraction and scattering from the disk. Thus the lifetime provided a more accurate picture of the cavity enhancement of the emitters while the enhanced collection rate resulted from a combination of increased collection efficiency and enhanced spontaneous emission from SiV centers.

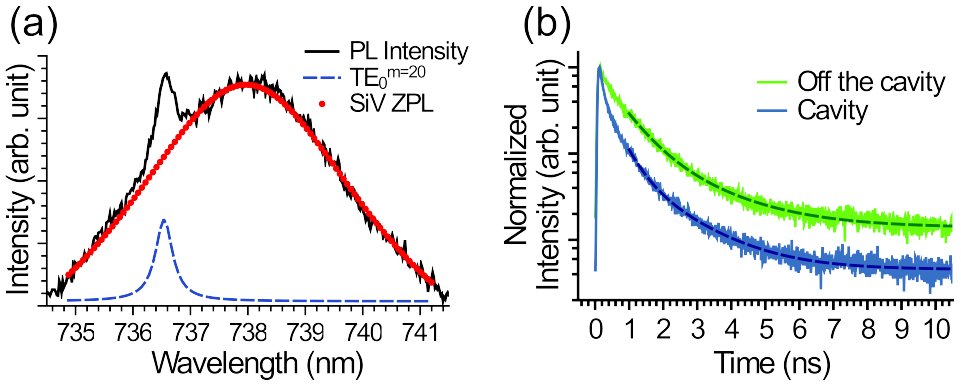

Figure 3.5.4: (a) Room temperature PL spectrum of the 1st order radial TE mode ($\mathrm{TE}_{o}^{m=20}$). The spectrum was background corrected. The Q factor was $\sim$ 2200 and spectral overlap with the ZPL of SiV centers was observed. The solid curve is the spectrum measured, the dashed curve is a Lorentzian fit of the cavity mode, and the dotted curve is a Lorentzian fit of the ZPL of SiV center. (b) Fluorescence lifetime measurement of SiV centers within microdisk resonators showed lifetime reduction from 1.83 ns to 1.48 ns, compared to the SiV centers in the diamond membrane, recorded at 18 K. The lifetime was fit to a bi-exponential decay (dashed lines) where reduction for both the fast and slow decay channel were observed.

The quality factors of ~ 2200 measured from the microdisks were comparable with values recently reported for a single crystal diamond micro-ring resonator [54] and a significantly higher value than devices made of nanocrystalline diamond [53] or milled by using a focused ion beam [83]. Examination of the PL data of Figure 3.5.1(a) showed the SiV peak sitting atop a broad band of luminescence, which was successively diminished as the composite diamond membrane was thinned. The broad band luminescence was likely due to other impurities within the membrane and could lead to material reabsorption and hence limited the Q of the cavity. Removal of that central region may also provide an increase in the observed Q as has been seen in other material systems [84].

Coupling of SiV defects to an optical cavity marks pivotal progress towards the realization of scalable diamond-based quantum photonics networks. Although demonstrated with an ensemble in this work, coupling of single emitters should also be possible using the techniques described here. Our approach enables the formation of optically thin single crystal membranes with good optical and structural properties. Such membranes can serve as the basis for microdisks and photonic crystal cavities as well as enable the construction of an integrated photonic network of coupled diamond cavities and waveguides[55]. The approach provides flexibility in both the formation of color centers, as well as flexibility in the geometry of optical cavities formed around those centers. We believe that further optimization of the fabrication steps, such as the use of high temperature annealing or further reduction of impurity absorption will produce high Qs and stronger emitter-cavity coupling. These initial results represent an important milestone in

the achievement of diamond-based cavity quantum electrodynamics.

3.6 Summary

Fabrication of high quality diamond membranes were demonstrated by performing a homo-epitaxial overgrowth on a template diamond membrane made using ion-slicing method. NV centers were incorporated in the overgrown membranes and showed good spin coherence properties. Other color centers could also be incorporated in the overgrown membranes by using different growth substrates. For example, SiV centers was observed in the overgrown membranes. With improved material quality, the device performance also improved ($Q \sim 3{,}000$ from microdisk made from the overgrown membranes compared to $Q \sim 500$ from microdisk made from template layer). The improved device performance allowed us to observe optical coupling between SiV centers with WGM. The overgrowth methods on diamond membranes together with fabrication of photonic devices served as a crucial step toward building a QIP platform using diamond. By using implantation techniques and further improvement in material growth could enable us to gain control over the concentration of color centers and the position of the color centers in diamond membranes [15, 16] and move toward integrated quantum photonic network.

4

Further control of material growth

4.1 Introduction

High quality diamond membranes were fabricated by performing homo-epitaxial overgrowth on the lifted-off diamond membranes. The overgrown membranes exhibited narrower Raman line (~ 2.5 cm^{-1}) compared to the lifted-off membranes which were ion damaged during lift-off process. Microdisk cavities fabricated from

the overgrown membrane also showed better Q ($Q \sim 3{,}000$) compared to microdisk cavities fabricated from the ion damaged membranes ($Q \sim 500$). The NV centers were incorporated in the overgrown membranes during growth. Spin coherence times were measured from ensembles of NV centers in the overgrown membranes. However, the concentration of the emitters was not controlled and the position of the NV centers were randomly distributed for the experiments described in chapter 3. In order to couple a single NV center to optical microcavities, we would like to have sample with diluted NV density. Therefore, having control over the NV density is crucial. In order to achieve this goal, we need a reactor with good isolation. Fortunately, through the collaborations with David Awschalom's and Ania Bleszynski Jayich's groups at UCSB, such a growth reactor was available. In this chapter, we describe our effort to control the NV density of diamond membranes by adjusting the growth condition.

Diamond growth with a ^{15}NV delta-doped layer near the surface has been demonstrated recently by the UCSB group [16]. Such growth control opens opportunities to place the emitter (NV centers) at the field maximum of the cavity mode. In the second part of this chapter, we show fabricated diamond membranes with a ^{15}NV delta-doped layer. The ^{15}NV delta-doped membranes were characterized using Raman spectroscopy and PL measurements and showed good material quality. These results are important steps toward deterministic placement of NV centers in diamond membranes so that maximum spatial overlap of a single NV center with cavity mode may be achieved.

4.2 Growth with high microwave power

4.2.1 Diamond growth without nitrogen doping

In the previous chapter, high quality diamond membranes were grown using the lifted-off diamond membranes as a template layer [19]. NV centers were observed from the overgrown diamond membranes despite there being no nitrogen flow during the overgrowth process. The incorporation of nitrogen was thought to be due to chamber leakage, which led to uncontrollable NV density in the overgrown membranes. In order to gain control of the density of NV centers, a diamond growth reactor with better isolation from the atmosphere was required. Such a diamond growth reactor was available through the collaboration with David Awschalom's group at UCSB. To test the cleanness of the growth chamber, a diamond thin film was first grown without the introduction of nitrogen gas.

Lifted-off diamond membranes were placed on a bulk diamond substrate before being put into the growth reactor. The growth condition is described in Table 4.2.1, and the total growth time was 16 minutes and 40 seconds. A SEM image of the growth surface is shown in Figure 4.2.1(a). The total membrane thickness was measured to be $\sim$ 2.8 μm using SEM. This corresponded to an overgrown layer thickness $\sim$ 1.1 μm and a growth rate $\sim$ 66 nm/min. The diamond surface remained smooth after growth, the r.m.s surface roughness of the growth surface was measured to be $\sim$ 5 nm using AFM (Figure 4.2.1(b)).

The membrane was then flipped and placed on the SiO_2-Si substrate. The tem-

Table 4.2.1: Growth condition of diamond membranes without nitrogen doping

Microwave power	Pressure	CH_4/H_2	Growth rate
3000 W	165 torr	4%	$\sim$ 66 nm/min

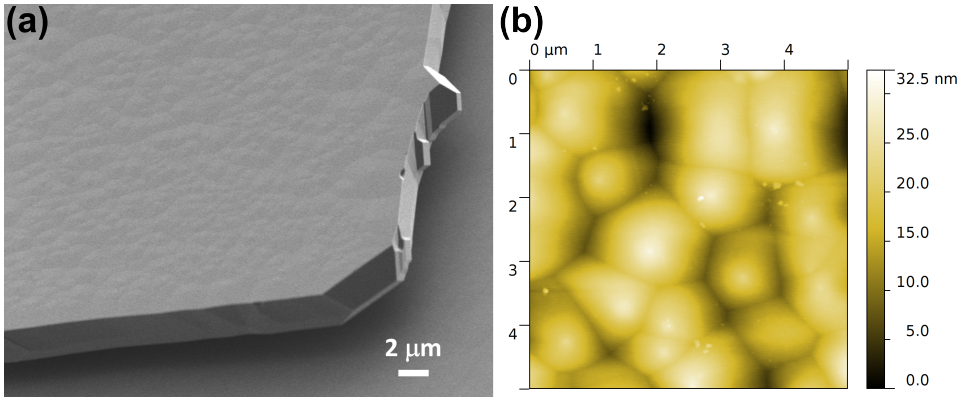

Figure 4.2.1: (a) A SEM image of the diamond membranes without nitrogen doping after diamond growth. (b) An AFM image of a 5 μm $\times$ 5 μm area on the overgrown membranes without nitrogen doping. The r.m.s surface roughness was measured to be $\sim$ 5 nm.

plate layer was etched away using a combination of Ar/Cl_2 based ICP-RIE followed by an O_2-ICP-RIE processes. The overgrown membrane showed no NV fluorescence (red curve in Figure 4.2.6) which indicated the growth reactor was indeed clean. The Raman peak exhibited narrow linewidth fitted using a Voigt function with FWHM of $\sim$ 2.5 cm^{-1} indicating that the material quality of the overgrown material was as good as the bulk diamond (Figure 4.2.2). Microdisk cavities were fabricated from the overgrown membranes by first depositing a 80 nm thick SiO_2 hard mask using PECVD. The devices were patterned using a 100 KeV electron beam writer with PMMA as the electron beam resist. The patterns were transferred using a SF_6 based ICP-RIE process to first etch the SiO_2 mask layer, followed by a

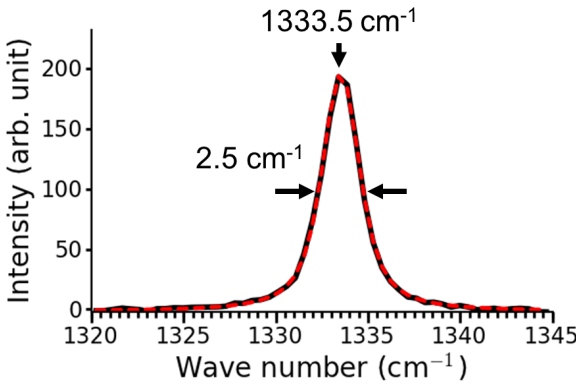

Figure 4.2.2: After removing the template layer, the Raman line of the overgrown material without nitrogen incorporation was measured. The Raman peak is fitted using Voigt profile and the FWHM of the Raman peak is measured to be $\sim$ 2.5 cm^{-1} which was closed to the bulk value.

O_2-ICP-RIE to etch through the diamond membranes. The remaining SiO_2 mask layer was removed using a SF_6 based ICP-RIE. The resulting microdisk cavity is shown in Figure 4.2.3. The disk was $\sim 2\mu$m in diameter and 300 nm thick.

The PL signal was collected using a confocal microscope with a 532 nm laser excitation. Whispering gallery modes were observed from the microdisk cavities. Since no NV fluorescence was observed, the WGMs were decorated by the background fluorescence from the diamond membrane (red curve in Figure 4.2.6). The WGMs were fitted with a Lorentzian profile with Q as high as 2,900 (Figure 4.2.4). Therefore, high quality optical micro-cavities could be fabricated from overgrown membranes without nitrogen doping.

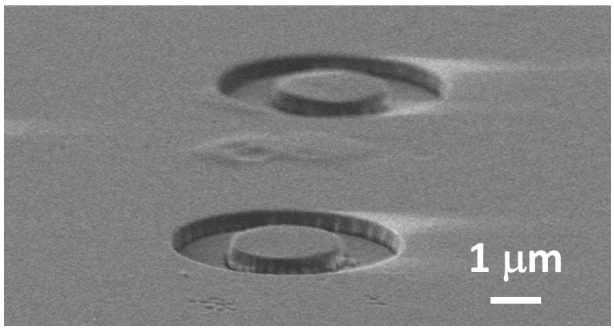

Figure 4.2.3: An SEM image of microdisk cavities fabricated from the overgrown membrane without nitrogen doping showed the cavity dimension with 2 μm diameter and thickness $\sim$ 300 nm.

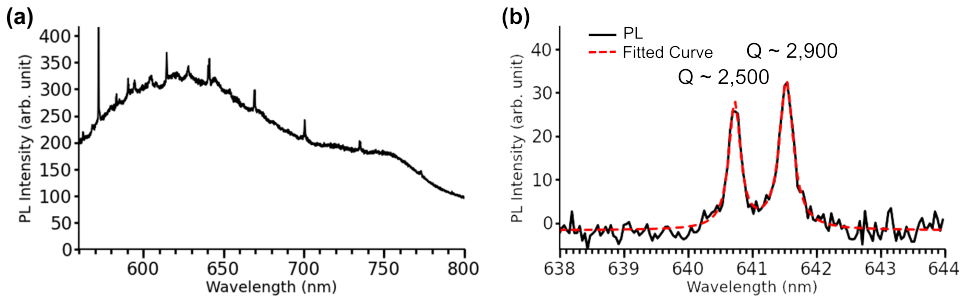

Figure 4.2.4: (a) Whispering gallery modes were observed from the microdisk cavities fabricated on overgrown membrane without nitrogen doping. (b) High resolution spectrum of the cavity modes showed Q $\sim$ 2,900, which was comparable to the microdisk cavities fabricated from overgrown material mentioned in chpater 3.

4.2.2 Diamond growth with nitrogen doping

In the previous subsection, high quality diamond membranes with diluted NV density were fabricated by performing an overgrowth without introduction of nitrogen gas. Ultimately, we would like to incorporate NV centers in the overgrown layer with controlled nitrogen doping. In this section, we characterized different growth conditions with nitrogen flow during growth.

Initially the same growth condition as the un-doped growth were applied for 8 minutes, a pulse of 0.1 sccm of nitrogen gas was injected for 4 seconds, then normal diamond growth was continued. The residual nitrogen gas from the pulsed N_2 flow became the nitrogen dopants for subsequent growth. Figure 4.2.5 shows SEM images of samples with varying time of diamond growth after pulsed N_2 flow. The surfaces of the membranes were roughened and therefore a different growth condition was required with nitrogen doping.

Diamond membranes with better surface properties were grown by reducing the CH_4/H_2 concentration to 1% and the microwave power from 3000 W to 2000 W with nitrogen flow throughout the growth process (Table 4.2.2). The PL signal from the nitrogen doped membranes showed more intense NV luminescence compared to the membranes without nitrogen doping. The Raman linwidth from the nitrogen doped membranes was still narrower (~ 3 cm^{-1}) than the template material (~ 9.9 cm^{-1}).

The ability to grow high quality diamond membranes with and without nitrogen

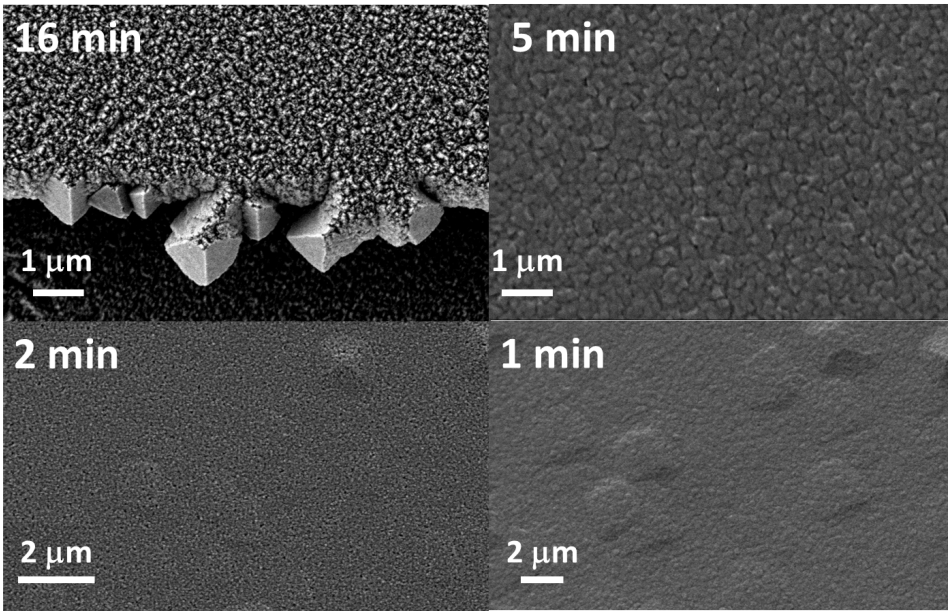

Figure 4.2.5: The SEM image of diamond surface with varying nitrogen incorporation. Clockwise from top right corner, the growth times after pulsed nitrogen flow were 16 minutes, 5 minutes, 1 minutes, and 2 minutes. Surface morphology was rough on all four samples, therefore, a different growth condition was needed.

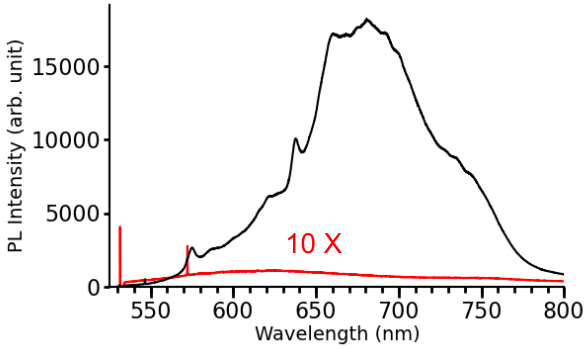

Figure 4.2.6: PL spectrum shows NV luminescence is much stronger from membranes with nitrogen doping (black curve) compared to membranes without nitrogen doping (red curve, 10× signal).

Table 4.2.2: Growth condition of diamond membranes without nitrogen doping

Microwave power	Pressure	CH_4/H_2	Nitrogen flow
2000 W	165 torr	1%	0.1 sccm

doping was an important step toward controlling the spatial distribution of NV center via growth methods. In the following section, we will introduce growing diamond thin film with a nitrogen delta-layer.

4.3 Delta-doping: toward controlled coupling

There are several requirements for achieving maximum coupling between a cavity mode and an emitter. First, the cavity mode resonance needs to have spectral overlap with the emitter. Resonant enhancement of the ZPL of color (single NV center or SiV centers) by tuning the cavity modes using Xe gas adsorption in cryogenic environment [54] or by using oxdiation methods [85] have been demonstrated. Second, the field maximum of the cavity mode needs to have spatial overlap with the emitter. Therefore, to have control over the position of the emitter is critical toward maximizing the coupling between a emitter and the cavity mode. There has been previous effort to created a N delta-doped layer in diamond using nitrogen implantation [15, 59]. However, ion damaged introduced during nitrogen implantation turns out to degrade the quality of NV centers created this way.

In this section, we describe our effort to fabricate diamond membranes with ^{15}N delta-doped layer incorporated in the middle of the membrane. The ^{15}N delta-doped layer was incorporated using a growth method, which should be a less dam-

aging way to introduce N into diamond [16]. We also changed strategies to grow diamond film on an ion-implanted bulk diamond sample instead of on the lifted-off membranes. This modification allows us to generate many more diamond membranes with a single growth. This modification also improves the stability during handling because the overgrown layer is attached to the bulk diamond during the growth process. The diamond membranes with ^{15}N delta-doped layer were lifted-off from the bulk substrate using the electrochemical etching described in chapter 2. The ^{15}N delta-doped diamond membranes showed r.m.s surface roughness of 1 nm and narrow Raman linewidth. We believed this is a first step toward controlled spatial coupling between the NV centers and the cavity mode by controlling the vertical position of the NV centers.

The starting material was an electronic grade type II-a CVD diamond sample with [N] < 5 ppb from Element Six^{TM}. A 1 MeV He^+ implantation with ion dose 5×10^{16} He^+/cm^2 was performed on the bulk diamond sample. The surface of the bulk substrate was smooth with r.m.s surface roughness $\sim$ 0.2 nm in a 10μm $\times$ 10 μm area (see figure 4.3.2(a)). A buffer layer was first grown on the implanted sample with isotopically purified $^{12}CH_4$ (99.999%). The growth rate was $\sim$ 8.2 $\pm$ 3.2 nm/hour [16]. A nitrogen doped layer was then grown by adding 10 sccm $^{15}N_2$ gas (98% isotopically purified) for 40 minutes, resulting in a $\sim$ 6 nm thick ^{15}N delta-layer. A cap layer was grown on the ^{15}N delta-layer using identical condition as the buffer layer. To create NV centers, vacancies were generated via electron irradiation (2 MeV energy with electron dose 10^{14} cm^{-2}), and the sample was annealed in forming gas at 850 °C for 2 hours. The surface was oxygen terminated

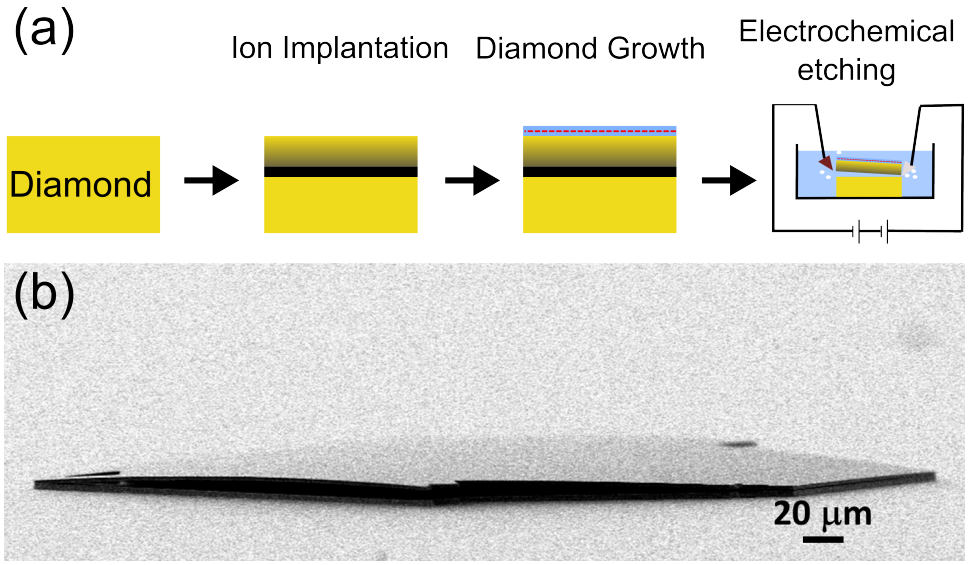

Figure 4.3.1: (a) The starting material is a bulk CVD diamond. A 1 MeV He^+ implantation was performed on the bulk diamond sample. Diamond membranes could be lifted off from the substrate using electrochemical etching process as described in chapter 2. (b) A SEM image of the lifted-off membrane transferred to a Si substrate.

by an acid process (H_2SO_4:HNO_3:$HClO_4$ = 1:1:1 at 200 °C for 30 minutes) in order to stabilize the NV centers in the negatively charged state. A 300 nm thick SiO_2 layer was deposited on the diamond samples using PECVD as a hard mask layer. The samples were then patterned with 400 μm $\times$ 400 μm mesas using photolithography. A SF_6 based ICP-RIE was applied to etch the SiO_2 hard mask layer, then an O_2-ICP-RIE was used to transfer the patterns by etching into the diamond sample. The SiO_2 hard mask was removed using a buffered oxide etchant (BOE) solution. We noted the surface after growth (r.m.s roughness $\sim$ 0.35 nm) was still smooth but it became slightly rougher compared to surface before growth, see Figure 4.3.2(b).

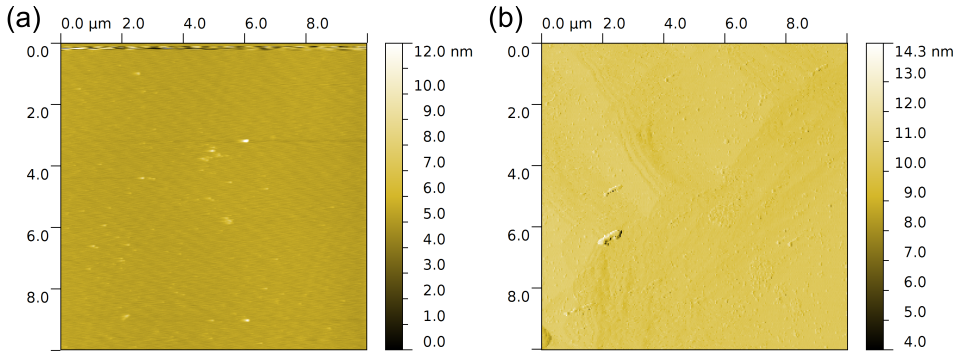

Figure 4.3.2: Surface roughness measurement before and after diamond overgrowth with delta-doped layer. (a) The r.m.s surface roughness before growth is 0.21 nm. (b) The r.m.s surface roughness after growth is 0.35 nm over a 10 μm $\times$ 10 μm area.

The growth conditions are listed in table 4.3.1 following an established growth recipe from the AIST group [86]. We noted the microwave power used here was much lower compared to the growth condition described previously. This was because the growth rate described in the previous sections ($\sim$ 66 nm/min) was much too high if we want to control the position of the ^{15}N delta-layer very precisely. By reducing the CH_4/H_2 ratio from 1% to 0.025%, the growth rate was slowed down to $\sim 8.2 \pm 3.2$ nm/hour [16].

Table 4.3.1: Growth condition of delta-doped diamond membranes

Microwave power	Pressure	CH_4/H_2	Growth rate
750 W	25 torr	0.1/400	$\sim$ 8 nm/hour

The ^{15}N delta-doped membranes were lifted-off from the bulk diamond samples by applying a 13 V bias using tungsten probe tips in ultra-pure DI water. The ^{15}N delta-doped membranes were than transferred to Si substrates as shown in Figure

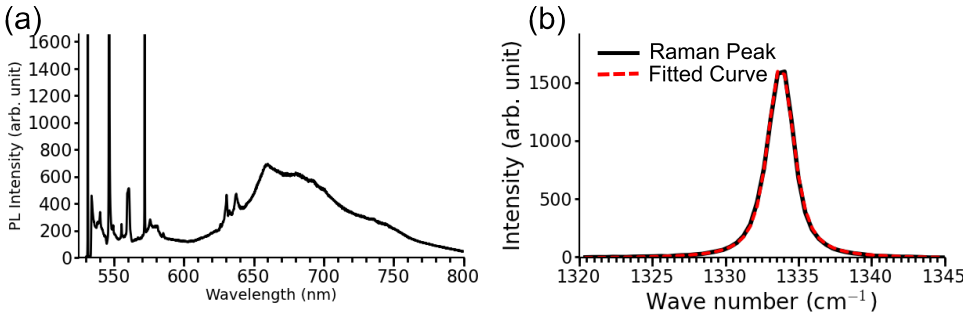

Figure 4.3.3: The delta-doped membranes exhibited NV luminescence and narrow Raman linewidth. (a) NV luminescence was observed from the delta-doped membranes. (b) The Raman peak from the delta-doped membranes was fitted with a Voigt profile, the FWHM was $\sim$ 2.2 cm^{-1}.

4.3.1(b). The template layer was etched off using an Ar-Cl_2 based ICP-RIE step followed by an O_2-ICP-RIE process. NV luminescence was observed from the ^{15}N delta-doped diamond membranes (Figure 4.3.3(a)) after thinning. The ^{15}N delta-doped diamond membranes also exhibited a narrow Raman peak fitted using a Voigt profile with FWHM $\sim$ 2.2 cm^{-1} as seen in figure 4.3.3(b).

4.4 Summary

In this chapter we report the various growth conditions that were tried in an attempt to create diamond membranes with controlled NV density and controlled position of NV centers. The first experiment showed diamond membranes grown without nitrogen flow showed no NV luminescence and a Raman line as narrow as the bulk diamond (FWHM $\sim$ 2.5 cm^{-1}). Then membranes with nitrogen doping was grown and the sample did show strong NV luminescence and narrow Raman line. This result showed that controlled NV density could be achieved. Microdisk

cavities fabricated from the un-doped membrane showed Q $\sim$ 2,900 which was comparable to the cavities fabricated previously on the high quality overgrown membranes. This result was encouraging because devices can be fabricated from membranes with controlled density of NV centers. Finally, to maximize the coupling strength, we would like to control the position of NV centers to have maximum spatial overlap with the cavity mode. Using recently demonstrated growth techniques [16], ^{15}N delta-doped membranes were grown on bulk ion implanted diamond samples. The ^{15}N delta-doped membranes were lifted off successfully from the bulk substrate. These delta-doped membranes grown at UCSB have smooth surface roughness (r.m.s roughness $\sim$ 0.35 nm), narrow Raman linewidth and exhibit NV fluorescence.

Table 4.4.1: Raman characteristics of diamond membranes

Sample	Raman peak (cm^{-1})	Raman linewidth (cm^{-1})
Bulk CVD diamond	1333.5 ± 0.33	2.3 ± 0.1
undoped membrane	1333.79 ± 0.12	2.54 ± 0.12
nitrogen doped membrane	-	-
delta doped membrane	1334.05 ± 0.09	2.17 ± 0.03
ion damaged diamond membrane	1331.0 ± 0.2	9.9 ± 0.4

Diamond membranes with different growth conditions have been characterized. We summarize the Raman characteristics of these membrane in table 4.4.1. It seems that most of the overgrown material exhibit Raman line as narrow as the bulk diamond, especially for the delta-doped membranes. These results further motivate us to fabricate optical cavities from the delta-doped membranes.

5

Single-crystal diamond photonic crystal cavities

5.1 Introduction

In previous chapters, we fabricated microdisk cavities with $Q \sim 3{,}000$ on overgrown diamond membranes. In order to further enhance coupling, we would like

to fabricate photonic crystal cavities which have smaller modal volumes compared to the WGM based cavities with similar cavity Qs. We have developed a technique to mechanically stamp diamond membranes onto PMMA which stabilized the membranes for further processing. Suspended structures could also be fabricated by selectively removing the PMMA layer underneath the cavity. Photonic crystal nano-beam cavities have been fabricated with $Q \sim 4{,}000$ and $V \sim 0.47\ (\lambda/n)^3$ in the near the NV ZPL emission (~ 640 nm) using a ^{15}N delta-doped diamond membrane described in chapter 4. Building photonic crystal cavities on diamond membranes with the ^{15}N delta-doped layer opens up opportunities to enhance optical coupling via deterministic spatial overlap between NV centers and the field maximum of the cavity mode. Cavity mode tuning on a diamond nano-beam cavity was also demonstrated using gas adsorption methods. The results in this chapter serve as an initial effort to achieve deterministic coupling both spectrally and spatially.

5.2 Fabrication of photonic cavities from diamond membranes

To fabricate the photonic crystal cavities, a suspended structure is required because the cavity Q is very sensitive to the surrounding environment. Mechanically stamping the diamond membranes onto PMMA enables us to create suspended structure. Bonding of the diamond membranes onto PMMA also enhances the process stability.

5.2.1 Bonding of diamond membranes

In the process of fabricating diamond membranes from bulk substrates, the lifted-off membranes experienced certain ion damage. The influence of ion damage was manifested in its broadened and shifted Raman peak [18]. The residual ion damage in the lifted-off membranes produced a built-in strain, which resulted in curving of the lifted-off membranes (Figure 5.2.1(a)). The large curvature of the diamond membranes often prevented further processing, including thinning of the membrane and the uniform removal of the damaged material. To minimize membrane curvature, the membrane was mechanically stamped onto a PMMA spin coated substrate (typically SiO2 or Si). The PMMA acted as a glue layer and held the membrane flat. A schematic diagram of the bonding process is shown in Figure 5.2.1(b). A flat membrane that has been stamped onto a PMMA layer and followed by a ICP-RIE thinning process is shown in Figure 5.2.1(c).

5.2.2 Undercut structures

Suspended structures could be fabricated by selectively removing the PMMA layer underneath the cavity. In this subsection, we used a 2D diamond photonic crystal cavity as an example. The diamond membranes were bonded to a PMMA layer and thinned using an ICP-RIE process. SiO_2 layer was deposited on the sample using PECVD and acted as a hard mask layer. The pattern was defined using electron-beam lithography with PMMA as the electron beam resist followed by an O_2-ICP-RIE process to etch into the diamond membranes. We noted that after etching

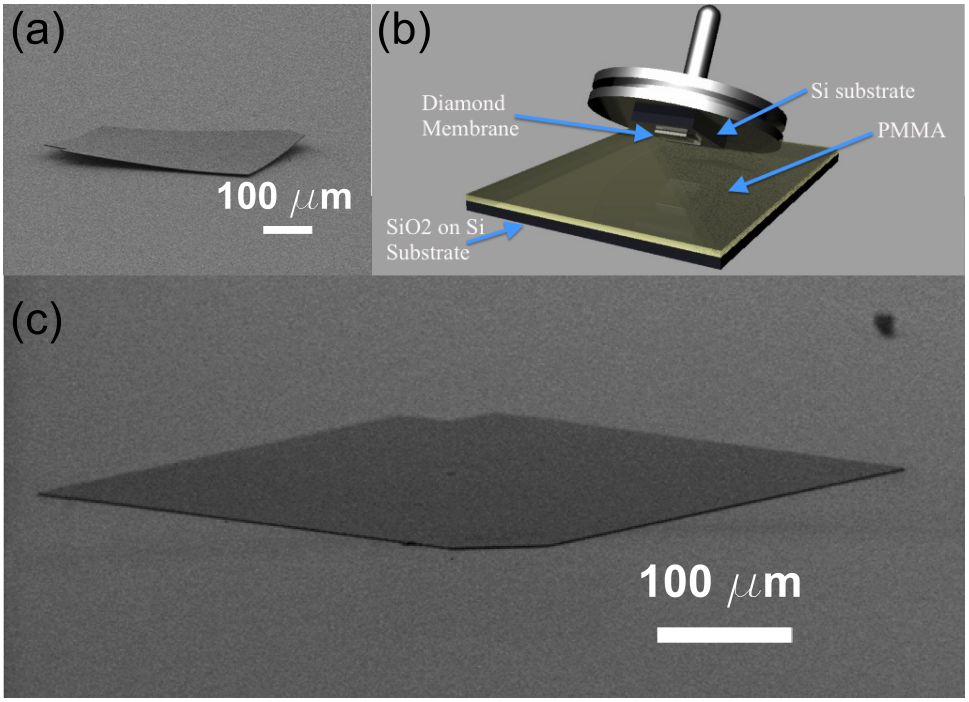

Figure 5.2.1: (a). Diamond membrane exhibiting curvature. (b) A schematic diagram of the stamping process. The diamond membrane is mounted on a sample holder and stamped onto a substrate coated with PMMA. (c) A stamped and thinned diamond membrane exhibiting uniform thickness without noticeable curvature.

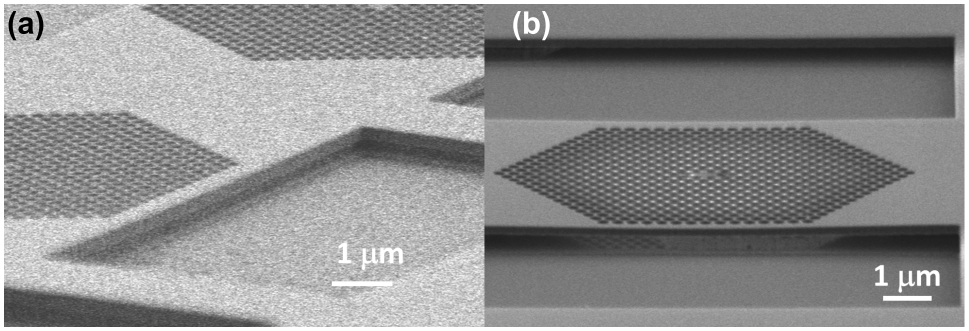

Figure 5.2.2: Undercut structure could be fabricated by selectively removal of PMMA underneath the cavity by immersing the sample in MIBK solution after etching. (a) SEM image of a photonic crystal cavity before undercut process. (b) SEM image of a photonic crystal cavity after undercut process.

the PMMA layer underneath the cavity still remains, which degrades the cavity Q (Figure 5.2.2(a)). In addition, the PMMA layer underneath the cavity region was also exposed during electron beam writing. Therefore, undercut structures could be fabricated by an extra developing step in methyl isobutyl ketone (MIBK) as the PMMA layer underneath the cavity was exposed after the ICP-RIE etching. An undercut structure was fabricated as can be seen in Figure 5.2.2(b).

5.3 Photonic crystal cavities fabricated on delta-doped membranes

We would like to build photonic crystal cavities on the ^{15}N delta-doped membranes. Photonic crystal cavities were chosen because of their high Q/V ratio [87, 88] which leads to enhanced light-matter interaction [89].

5.3.1 Design of nano-beam cavities

The choice of cavities in this section were 1-D photonic crystal nanobeam cavities. There has been many experimental demonstrations of nanobeam cavities with high Q/V ratio in Si [90] and even in materials with relatively low index contrast such as Si_3N_4 [91]. The nanobeam cavities consist of a tapered region and a Bragg mirror region. High Q designs have been demonstrated by reducing the mode mismatch between the mirror Bloch mode and the waveguide mode [92]. The design principle used in this work is linearly tapering the lattice constants to achieve gradual conversion of the Bloch mode profile and reduce mode mis-match [93–95].

The nanobeam cavity presented here consists of a tapered region sandwiched between a Bragg mirror region with 10 cells on each side. The tapered region has 4 cells on each side that are mirror symmetrical along the y-axis with no missing hole. The lattice constants of each cell were linearly tapered from a to 0.84 a (Figure5.3.1(a)). The beam width (w = 1.25 a) and r/a (r/a = 0.32) ratio were fixed for both the tapered region and the Bragg mirror region. The holes in the tapered region were elliptical because the lattice constants were linearly tapered while the r/a ratio were maintained which made the hole radius in the minor axis (y-axis) linearly reduced while the hole radius in the major axis (x-axis) remained the same (r_x = 0.32 a).

A FDTD simulation was performed using a commercial software (Lumerical Solutions). By looking at the x-z field intensity profile of the cavity mode, we noted the field maximum was in the middle of the device layer in the z-direction which

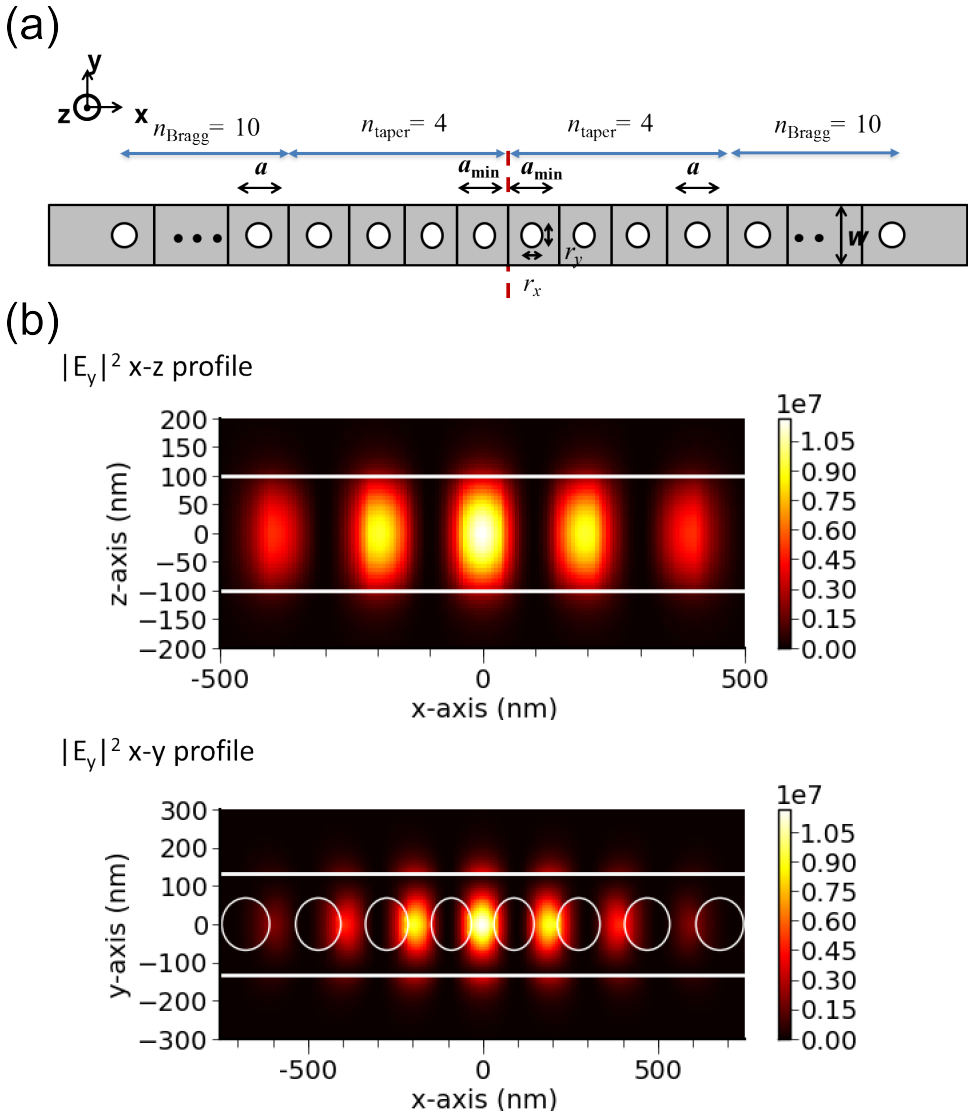

Figure 5.3.1: (a) The nano-beam cavities consisted of a Bragg region and a cavity region on each side that are symmetrical in the y-axis. There was no missing hole inbetween the cavity regions. The nano-beam width and the r/a ratio for each hole was fixed. In the cavity region, the lattice constant was linearly reduced from a to a_{min} therefore, the holes in the cavity region are elliptical as the hole diameter in the minor axis reduced with the lattice constant. (b) Electric field intensity profile of the cavity mode. The modal volume of the cavity mode was $\sim 0.47\ (\lambda/n)^3$.

overlapped with the ^{15}N delta-layer. The cavity Q$\sim$ 270,000, with modal volume $\sim$ 0.47 $(\lambda/n)^3$ was calculated using FDTD simulation. We only used 4 linear tapered cells on each side because we wanted a compromise between fabrication error and theoretical Q (diameter in the minor axis varied by 7.3 nm between each layer). The Q of the cavity can be higher by using linear tapered structures with finer variation of the lattice constants (e.g. cavity layers with 8 linearly tapered lattices showed Q$\sim 9 \times 10^5$, where the diameter in the minor axis varied by 3.2 nm between each layer) as shown in table 5.3.1.

Table 5.3.1: Design parameters of nanobeam cavities

a	r/a	w/a	n_{taper}	n_{Bragg}	Q	δr
213 nm	0.32	1.25	4	10	270,000	3.65 nm
217 nm	0.32	1.25	8	10	931,000 $\pm$ 49,000	1.6 nm

5.3.2 Fabrication of nano-beam cavities

Figure 5.3.2 describes the processing steps to fabricate delta-doped membranes. The starting material was a diamond film grown on an He^+-implanted bulk diamond sample described in Chapter 4. A 65 nm buffer layer was grown on the bulk substrate followed by a ^{15}N delta-doped layer growth that was $\sim$ 6 nm and a 65 nm cap layer was grown on top of the ^{15}N delta-doped layer. The diamond membranes were lifted off from the bulk substrate using the electrochemical etching method described in chapter 2. The diamond membrane was transferred to a Si substrate. The membrane was then mechanically stamped onto a PMMA spin coated Si substrate. The membrane was thinned to $\sim$ 250 nm thick using an argon-

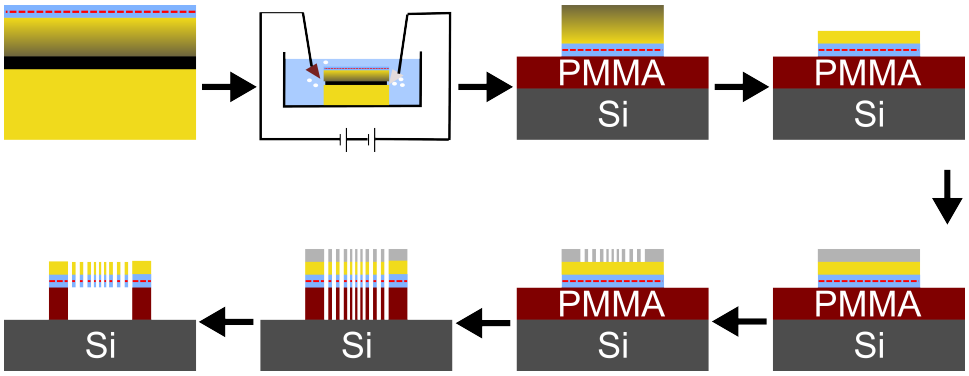

Figure 5.3.2: Photonic crystal cavities were fabricated on the nitrogen delta-doped membranes. The starting material was a bulk diamond with 1 MeV He^+ implantation (dose 5×10^{16} He^+/cm^2). Diamond growth with ^{15}N delta-layer was performed using a PECVD reactor. The diamond membranes were then lifted-off using an aqueous electrochemical etching process. The diamond membranes were flipped and stamped onto a double layer of PMMA on Si that was $\sim$ 1.2 μm thick. The template layer was facing up. The membranes were thinned to $\sim$ 250 nm using an Ar-Cl_2 based ICP-RIE process followed by an O_2-ICP-RIE process. Electron beam lithography was employed to pattern the cavities using a floating oxide as the e-beam resist. The HSQ based resist served as the hard mask and the pattern was subsequently transferred using O_2-ICP-RIE. The remaining hard mask was then removed by dipping the sample in buffered oxide etchant.

chlorine based ICP-RIE followed by an O_2-ICP-RIE. The pattern was written using a 125 KeV electron-beam writer (Elionix-F125) with a negative tone hydrogen silsesquioxane (HSQ) based resist (XR-1541, Dow Corning). The HSQ based resist was then used as the hard mask for subsequent O_2-ICP-RIE to define the nanobeam patterns. The residual hard mask was removed using a BOE solution. The SEM images of the device are shown in Figure 5.3.3, where the thickness of the device was measured to be $\sim$ 250 nm. We note that the cavity to substrate separation was > 1 μm as the 2 layer PMMA underneath the beam was etched by the O_2

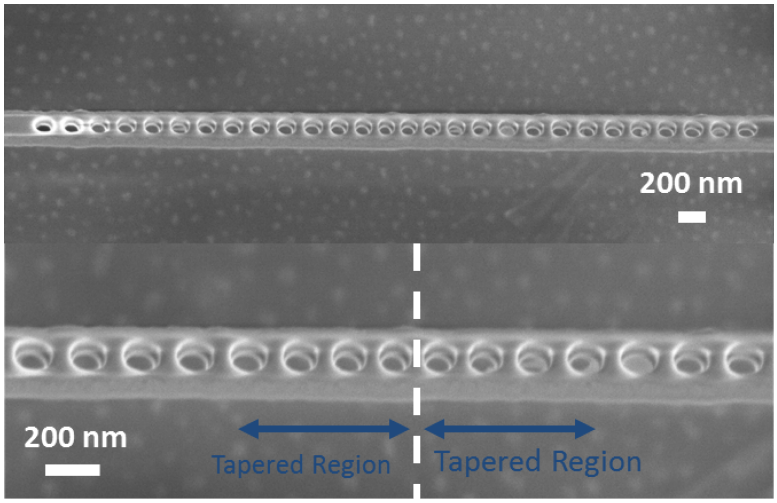

Figure 5.3.3: Nano-beam cavities with lattice constant a = 213 nm and thickness ∼ 250 nm were fabricated. The SEM image shows the tapered cavity region and the Bragg layers.

plasma during the etching process and formed the undercut structure.

5.3.3 Optical characterization of nano-beam cavities

The resulting nano-beam cavities were characterized using a confocal microscope with a 100 ×, 0.95 numerical aperture objective with a 532 nm laser excitation at room temperature. The photoluminescence signal was collected through the same objective normal to the substrate. The cavity mode was fitted with a Lorentzian profile and Q as high as 4,000 was observed. Cavity mode (Q ∼ 2,900) with spectral overlap was measured from a different cavity. Such results suggested high Q/V ratio diamond cavity structures with spectral overlap to the NV ZPL could be fabricated on the delta-doped membranes.

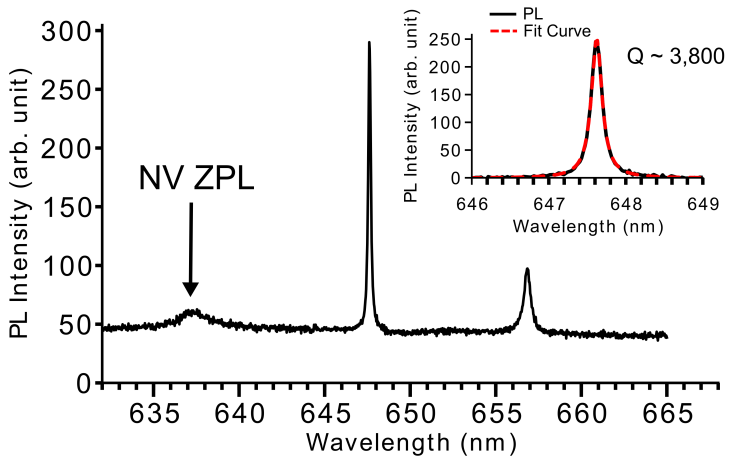

Figure 5.3.4: Photoluminescence was measured using a confocal microscope with 532 nm laser excitation. The cavity mode resonance was fitted with a Lorentzian profile with Q $\sim$ 3,800. The ZPL of NV^- was observed as well.

The Raman peak measured from the nano-beam cavities was best fitted with a 2 Voigt profile. One peak centered at 1333.36 cm^{-1} with FWHM = 2.23 cm^{-1} corresponded to the Raman peak from overgrown membrane and another peak centered at 1331.98 cm^{-1} with FWHM = 5.39 cm^{-1} correspond to Raman peak from the template material. This result was not surprising because the membrane thickness ($\sim$ 250 nm) was thicker than the overgrown membrane (designed to be $\sim$ 136 nm thick). Therefore, the cavity was a composite of the overgrown membrane and the template material. The long growth process ($\sim$ 25 hours) at high temperature (850 ^{circ}C) could serve as a long annealing process which restores the less damaged part of the template material. Therefore, the composite material can still exhibit cavity Q$\sim$ 4,000.

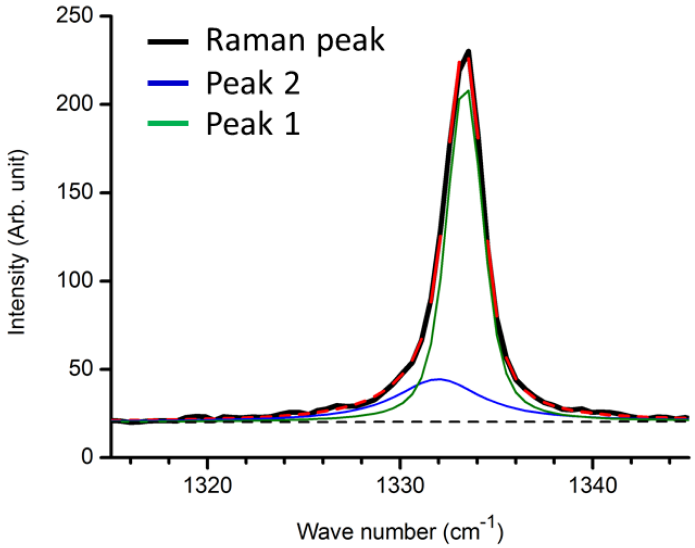

Figure 5.3.5: The Raman peak measured from the nano-beam cavities was best fitted with two Voigt profiles. Peak 1 is centered at 1333.36 cm^{-1} with FWHM = 2.23 cm^{-1} (green curve). Peak 2 is a broad peak shifted to the lower wave number centered at 1331.98 cm^{-1} with FWHM = 5.39 cm^{-1} (blue curve).

5.3.4 Cavity mode tuning with gas condensation

The ability to tune the cavity is crucial in order to have the cavity mode in resonance with the ZPL emission of the NV centers because it is rare to have fabricated cavities with the exact same resonance wavelength matching the emitter. Resonance enhancement of NV^- ZPL has been achieved in both diamond micro-ring resonators [54] and photonic crystal cavities [56] using Xe gas adsorption in a cryogenic environment. Here, we present our initial attempt for cavity tuning using a similar concept by gas adsorption using nitrogen. Nitrogen gas was injected into a liquid helium cooled environment such that the temperature of the device was lower than the freezing point of nitrogen. Therefore, nitrogen gas near the device condensed and adsorbed onto the surface of the device. The addition of extra material on the cavity increased the cavity volume and caused the cavity mode to shift to longer wavelengths.

In this experiment, the cyrostat (Janis) was modified by Kasey Russell and Alex Woolf in our lab. A small hole was punched through the top cover of the cryostat and a small gas tube was connected. The gas tube was mounted in a position such that it would be near the sample and nitrogen gas was fed through a flow controller. We looked at a nano-beam cavity with cavity mode at 602 nm with $Q \sim$ 1,000 and cooled it down to 8 K. Cavity mode tuning to as far as $\sim$ 626 nm was achieved with adsorbed nitrogen (Figure 5.3.6). However, the cavity Q degraded to $\sim$ 500 near 626 nm and the mode was not observable with further tuning. After warming up the sample back to room temperature, cavity mode with $Q \sim$ 1,000 was still

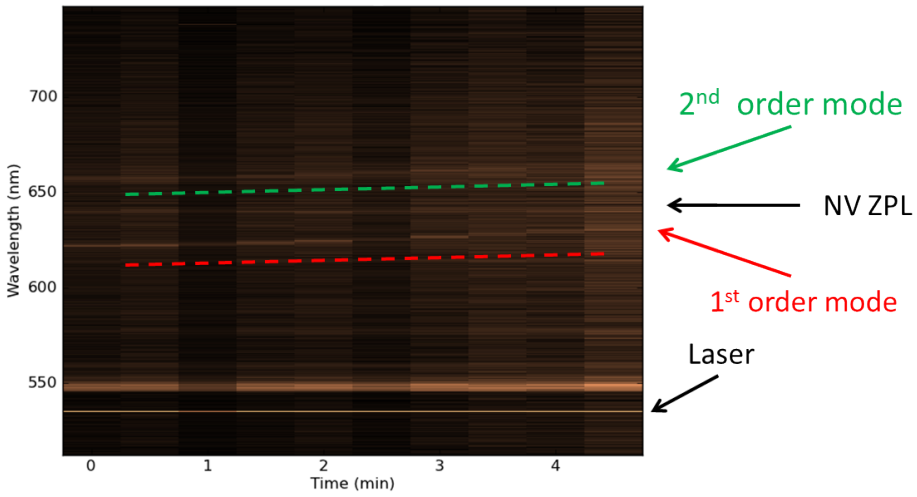

Figure 5.3.6: The cavity mode could be tuned using nitrogen adsorption in a cryogenic environment. The sample was first cooled to 8 K and then nitrogen gas was injected through a needle near the sample.

observed with no noticeable resonance shift.

In order to tune the cavity mode closer to the NV^- ZPL, we either need to etch the diamond with an O_2 plasma to blue shift the cavity mode or deposit SiO_2 via atomic layer deposition to red shift the cavity mode. Then the gas adsorption technique described above could be applied for fine tuning of the cavity mode.

5.4 Summary

Fabrication of suspended cavity structures was demonstrated by mechanically stamping the diamond membranes on a PMMA layer which was selectively etched. Diamond photonic crystal cavities with $Q \sim 4{,}000$ and modal volume $\sim 0.47\ (\lambda/n)^3$ were fabricated on ^{15}N delta-doped membranes and are an encouraging first step

towards coupling diamond cavities with NV centers in predetermined positions. Cavity tuning using nitrogen adsorption was demonstrated. These results are important steps towards enhanced coupling between photonic crystal cavity modes and NV centers.

6

Conclusion and Future works

6.1 Conclusions

Much progress has been made in the field of diamond photonics since the start of this thesis [12, 42]. Engineered photonic structures have enabled enhanced light collection efficiency from NV centers [45, 46]. Fabrication of high quality single-crystal diamond photonic devices have enabled observation of resonant enhance-

ment of NV ZPL [54, 56] and integrated photonic structures [57, 58]. Much of these progresses relies on the better understanding on material processing in diamond.

Most of the proof of principle demonstrations until now were done in NV centers in synthetic diamond that are randomly distributed. In order to build a scaled-up system using NV centers in diamond, it is important to have control over the position of the NV centers. Controlling the position of NV centers with nm-scale resolution was demonstrated using ion implantation approach and lithographic masking [15]. More recently, controlling the position of NV centers using diamond growth was also demonstrated [16]. Such tailored material may serve as an important step toward having good NV centers with controlled position.

In this thesis, we presented a method to fabricate high quality single-crystal diamond membranes through an ion-slicing method combined with a homo-epitaxial diamond growth [18, 19]. Optical micro-cavities with Q($\sim$ 3,000) similar to the ones exhibited resonant enhancement of NV ZPL are fabricated using such approach further demonstrate the viability of this technology. The key advantage of the approach we developed here is that the membrane material can be tailored towards specific needs. One example is by growing diamond membranes with incorporated SiV centers, evidenced by observing optical coupling of SiV centers with a microdisk cavity [17]. By fabricating a thin diamond membrane ($\sim$ 1.7μm thick) and overgrowing diamond membranes with controlled NV positions. Photonic crystal cavities with Q$\sim$ 4,000 were fabricated from such material which serves as an exciting first step to make a scalable diamond photonic network using such

approach.

6.2 Outlooks

With the tremendous progress that has been made in the field of diamond photonics, the field of diamond photonics is still at an early stage compared to silicon photonics or photonics using III-V semiconductors. Improvements in better material processing and the better understanding of the material growth are required to achieve what people dream up this system to be. We would like to point out some future directions using the techniques developed in this thesis.

6.2.1 Toward integrated diamond quantum photonics

One important issue towards scalability is to deterinisitically positioning of the NV centers. Deterministic positioning of a single NV center and a photonic crystal cavities has been demonstrated in using the hybrid approach, which use optical cavities made from other material to couple to the NV centers. Techniques were developed by attaching a nano-diamond on an AFM tip which provide a versatile tool to position the NV centers in the x-y directions. Using such techniques experiments has been done [96]. Other approach by scanning the photonic crystal cavities to have spatial overlap with the NV centers has also been demonstrated [97]. However, such schemes relied on optical coupling between a single NV center with the evanescent field of the cavity which limits the coupling strength.

Fabrication of single-crystal diamond cavities with the NV centers embedded within offer opportunities to achieve maximum spatial overlap between a single

NV center and the cavity mode. As illustrated in figure 6.2.1, by first fabricating a ^{15}NV delta-doped membranes with diluted ^{15}NV and the ^{15}NV delta-layer in the middle of the membranes in the z-direction (same as the membranes fabricated in chapter 4), the x-y position of the isolated NV centers can be identified using a scanning confocal microscope. The ^{15}NV centers in the delta-doped layer can be distinguished using ESR measurements because the ESR frequency of ^{15}NV is different from ^{14}NV. Photonic crystal cavities with field maximum overlapping with the isolated ^{15}NV can be fabricated by aligning and writing with electron beam lithography. Similar approach has been achieved in GaAs cavity with InAs quantum dot (QD) which led to strong coupling between cavity mode and a single QD [37].

Ultimately, fabrication of an array of NV centers with precise 3 D positioning will be desired. The NV centers in the N delta-doped membranes are formed by first creating vacancies in the membranes using an electron irradiation followed by a thermal annealing step to move the vacancies near the N delta-doped layer. Therefore, we can instead performing an electron irradiation through a lithographic patterned mask similar to the previous approach using a nitrogen implantation [15]. Such approach could allow NV centers be formed in a predetermined position defined in all three dimensions. By avoiding the nitrogen implantation, high quality NV could be generated using this method. Cavities can then be fabricated using approach mentioned in the previous paragraph. Such approach may further increase the scalability of diamond photonic network.

Another goal is to fabricate diamond membranes with uniform thickness for

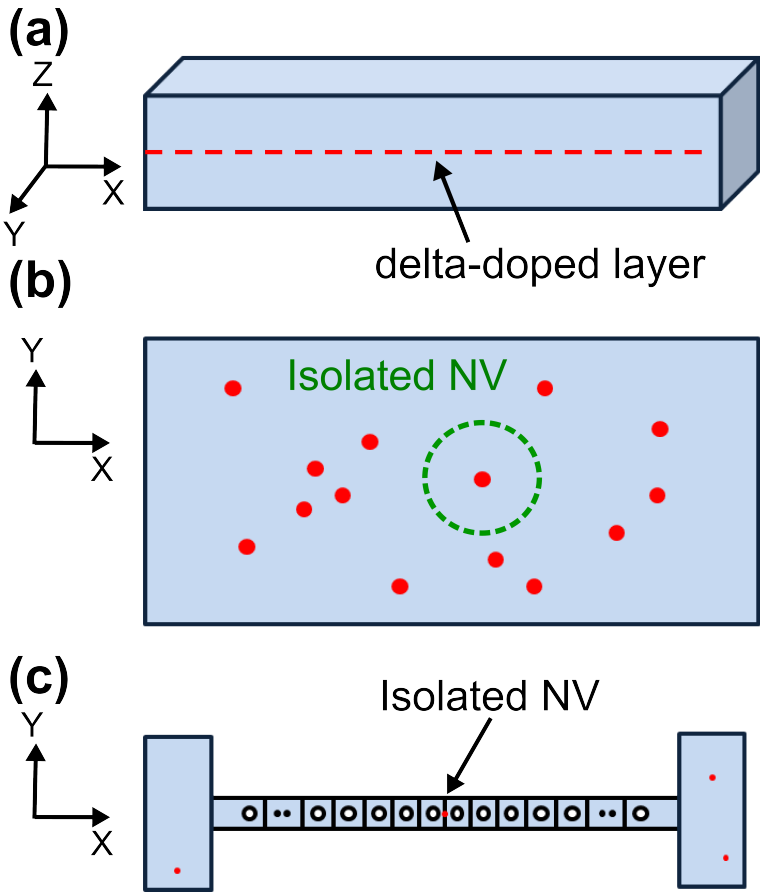

Figure 6.2.1: Maximum spatial overlap could be achieve by fabricating caivties on delta-doped membranes. (a) Diamond membranes with NV delta-doped layer in the middle can be fabricated. (b) Isolated NV (green circle) could be identified using scanning confocal microscopy and ESR measurement. (c) Device could be made around the isolated NV using alignment write. Such approach is similar to the deterministic coupling approach demonstrated by Kevin Hennessy in InAs quantum dots system [37].

scalable diamond photonic structures. Diamond membrane thickness can vary by $\sim$ 100 nm across 400 μm range. This is not a problem for demonstration of a single device, however, such variation makes it difficult to fabricate integrated photonic network since the thickness variation will influence the resonance wavelength of the optical cavities. The reason of the membrane thickness variation is thought to be due to etch non-uniformity during the ICP-RIE diamond thinning process. Therefore, by reducing the template membrane thickness less material would need to be etched. The template membrane thickness is determined by the implantation conditions, therefore, its thickness can be reduced by choosing a lower implantation energy and heavier ion. In figure 6.2.2, SRIM simulation indicates a template membrane thickness $\sim$ 400 nm can be fabricated. Diamond membranes with uniform thickness may be fabricated by growing on diamond with lower implantation energy following fabrication procedures introduced in chapter 3.

6.2.2 Bottom up diamond photonics

High quality diamond can be grown on the diamond membranes. By performing diamond growth through lithographic patterned mask, photonic structures can be fabricated using a bottom up approach. Devices such as photonic crystal laser has been fabricated using such approach in III-V semiconductors [98]. The process schematic is illustrated in figure 6.2.3(a), a diamond membrane is used as the growth template, a SiO_2 layer is depoisted on the membrane. The pattern is defined using electron beam lithography and followed by a SiO_2 etching. A diamond overgrowth is then applied, the structures are then bonded to a dielectric substrate.

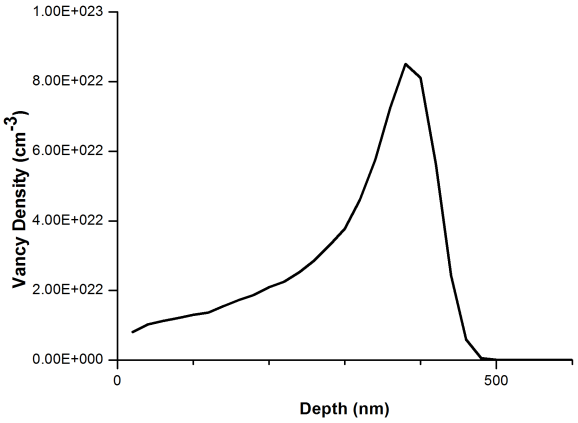

Figure 6.2.2: SRIM simulation of vacancy profile of carbon implantation in diamond with 385 KeV and ion dose 6×10^{15} ion/cm^2. The heavily damaged layer is $\sim$ 400 nm into the substrate corresponding to a template membrane thickness $\sim$ 400 nm.

and the template membrane is removed using ICP-RIE process. A first experiment on diamond growth through the aperture is depicted in Figure 6.2.3(b). An array of diamond pillar is grown on bulk diamond with patterned SiO_2 mask, the SiO_2 was subsequently removed using BOE and diamond pillar array could be observed. This technique can be used to grow photonic crystals, microdisks, or other photonic structures.

6.2.3 Other applications for diamond membranes

Diamond has a high Young's modulus and low mass density which also makes it an interesting material for mechanical applications [99]. By using a diamond on insulator structure through bonding of diamond membranes, single-crystal diamond mechanical resonators can be fabricated and exhibit high Q factor even at room

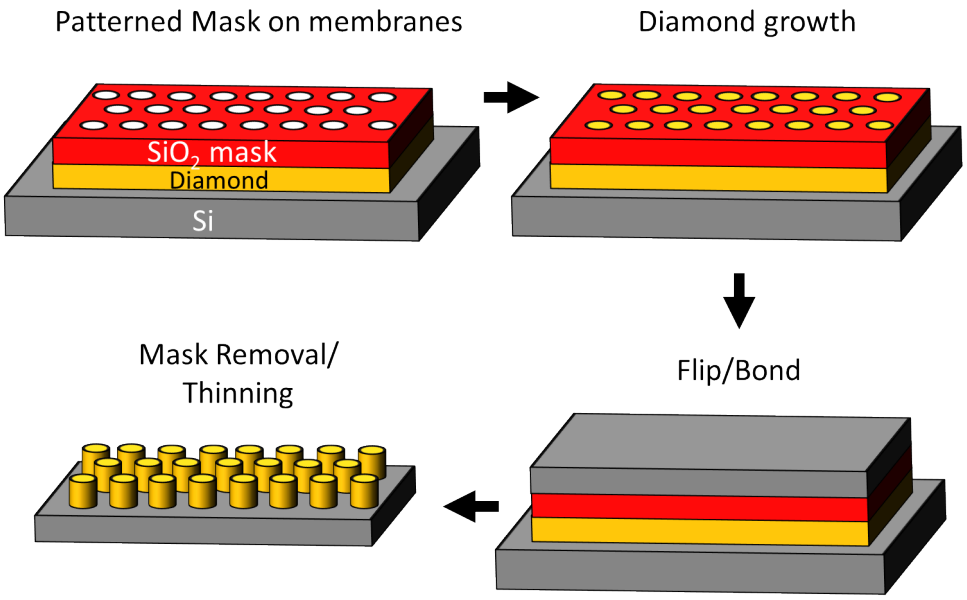

Figure 6.2.3: Diamond growth through a masked layer enables fabrication of photonic structures using bottom up approach. (a) A SiO_2 (red) is deposited on a diamond membrane (yellow) using PECVD. The pattern is defined by electron beam lithography followed by a SF_6 based ICP-RIE process. Diamond overgrowth is subsequently applied to growth through patterns. The structure is then flipped and bonded to dielectric layer and the template membrane is removed by O_2-ICP-RIE, leaving behind a diamond pillar array. (b) An SEM image of initial effort growing an array of diamond pillars through a SiO_2 mask layer. Courtesy of Igor Aharonovich.

temperatures [100, 101]. Such results open up opportunities to incorporate NV centers in diamond mechanical resonators for magnetic field sensing [102, 103], ground state cooling [104] or mechanical control over spin state [105]. The strategies to position NV centers in the diamond membranes can be applied to fabricate diamond mechanical resonators with NV centers in desired positions.

We believe there are many other applications where high quality diamond membranes can be useful, not limited only to photonic applications. We are hoping the techniques developed in this thesis will see wide-spread applications as material processing, physics, device fabrication of diamond get more mature.

References

[1] D. D. Awschalom, R. Epstein, R. Hanson, *Scientific American* **297**, 84 (2007).

[2] D. D. Awschalom, L. C. Bassett, A. S. Dzurak, E. L. Hu, J. R. Petta, *Science* **339**, 1174 (2013).

[3] G. Balasubramanian, *et al.*, *Nature Materials* **8**, 383 (2009).

[4] C. Kurtsiefer, S. Mayer, P. Zarda, H. Weinfurter, *Physical Review Letters* **85**, 290 (2000).

[5] A. Beveratos, R. Brouri, T. Gacoin, J.-P. Poizat, P. Grangier, *Physical Review A* **64** (2001).

[6] F. Jelezko, T. Gaebel, I. Popa, A. Gruber, J. Wrachtrup, *Phys. Rev. Lett.* **92** (2004).

[7] E. Togan, *et al.*, *Nature* **466**, 730 (2010).

[8] H. Bernien, *et al.*, *Physical Review Letters* **108**, 043604 (2012).

[9] A. Sipahigil, *et al.*, *Physical Review Letters* **108**, 143601 (2012).

[10] H. Bernien, *et al.*, *Nature* **497**, 86 (2013).

[11] L. Childress, R. Hanson, *MRS Bulletin* **38**, 134 (2013).

[12] M. Lončar, A. Faraon, *MRS Bulletin* **38**, 144 (2013).

[13] K. J. Vahala, *Nature* **424**, 839 (2003).

[14] P. M. Petroff, A. Lorke, A. Imamoglu, *Physics Today* **54**, 46 (2001).

[15] D. M. Toyli, C. D. Weis, G. D. Fuchs, T. Schenkel, D. D. Awschalom, *Nano Letters* **10**, 3168 (2010).

[16] K. Ohno, *et al., Applied Physics Letters* **101**, 082413 (2012).

[17] J. C. Lee, I. Aharononvich, A. P. Magyar, F. Rol, E. L. Hu, *Optics Express* **20**, 8891 (2012).

[18] A. P. Magyar, *et al., Applied Physics Letters* **99**, 081913 (2011).

[19] I. Aharonovich, *et al., Advanced Materials* **24**, OP54 (2012).

[20] L. T. Hall, *et al., Sci Rep* **2** (2012). PMID: 22574249 PMCID: PMC3348610.

[21] L. P. McGuinness, *et al., Nat Nano* **6**, 358 (2011).

[22] V. N. Mochalin, O. Shenderova, D. Ho, Y. Gogotsi, *Nat Nano* **7**, 11 (2012).

[23] A. Zaitsev, *Optical Properties of Diamond* (Springer, 2000).

[24] I. Aharonovich, *et al., Rep. Prog. Phys.* **74**, 076501 (2011).

[25] E. Neu, *et al., New Journal of Physics* **13**, 025012 (2011).

[26] I. Aharonovich, *et al., Physical Review B* **81**, 121201 (2010).

[27] J. H. N. Loubser, J. A. v. Wyk, *Reports on Progress in Physics* **41**, 1201 (1978).

[28] A. Dräbenstedt, *et al., Physical Review B* **60**, 11503 (1999).

[29] N. Aslam, G. Waldherr, P. Neumann, F. Jelezko, J. Wrachtrup, *New Journal of Physics* **15**, 013064 (2013).

[30] A. Gruber, *et al., Science* **276**, 2012 (1997).

[31] A. Nizovtsev, *et al., Physica B: Condensed Matter* **340–342**, 106 (2003).

[32] F. Jelezko, *et al., Applied Physics Letters* **81**, 2160 (2002).

[33] J. Harrison, M. Sellars, N. Manson, *Journal of Luminescence* **107**, 245 (2004).

[34] R. Hanson, D. D. Awschalom, *Nature* **453**, 1043 (2008).

[35] C. G. Yale, *et al.*, *Proceedings of the National Academy of Sciences* **110**, 7595 (2013). PMID: 23610403.

[36] D. K. Armani, T. J. Kippenberg, S. M. Spillane, K. J. Vahala, *Nature* **421**, 925 (2003).

[37] K. Hennessy, *et al.*, *Nature* **445**, 896 (2007).

[38] A. Yariv, P. Yeh, *Photonics: Optical Electronics in Modern Communications* (Oxford University Press, USA, 2006), 6th edn.

[39] K. Srinivasan, Semiconductor optical microcavities for chip-based cavity QED, Ph.D. thesis, California Institute of Technology, Pasadena, California (2006).

[40] E. M. Purcell, *Physical Review* **69**, 681 (1946).

[41] B. Gayral, *Ann. Phys. Fr* **26** (2001).

[42] I. Aharonovich, A. D. Greentree, S. Prawer, *Nat Photon* **5**, 397 (2011).

[43] C. Santori, *et al.*, *Nanotechnology* **21**, 274008 (2010).

[44] B. J. M. Hausmann, *et al.*, *physica status solidi (a)* **209**, 1619–1630 (2012).

[45] T. M. Babinec, *et al.*, *Nat Nano* **5**, 195 (2010).

[46] J. P. Hadden, *et al.*, *Applied Physics Letters* **97**, 241901 (2010).

[47] P. Neumann, *et al.*, *Science* **329**, 542 (2010).

[48] L. Robledo, *et al.*, *Nature* **477**, 574 (2011).

[49] L. C. Bassett, F. J. Heremans, C. G. Yale, B. B. Buckley, D. D. Awschalom, *Physical Review Letters* **107**, 266403 (2011).

[50] H. J. Kimble, *Nature* **453**, 1023 (2008).

[51] S. C. Benjamin, B. W. Lovett, J. M. Smith, *Laser & Photonics Reviews* **3**, 556–574 (2009).

[52] C. F. Wang, *et al.*, *Applied Physics Letters* **90**, 081110 (2007).

[53] C. F. Wang, *et al.*, *Applied Physics Letters* **91**, 201112 (2007).

[54] A. Faraon, P. E. Barclay, C. Santori, K.-M. C. Fu, R. G. Beausoleil, *Nature Photonics* **5**, 301 (2011).

[55] B. J. M. Hausmann, *et al.*, *Nano Letters* **12**, 1578 (2012).

[56] A. Faraon, C. Santori, Z. Huang, V. M. Acosta, R. G. Beausoleil, *Phys. Rev. Lett.* **109**, 033604 (2012).

[57] A. Faraon, *et al.*, *New Journal of Physics* **15**, 025010 (2013).

[58] B. J. M. Hausmann, *et al.*, *Nano Letters* (2013).

[59] B. J. M. Hausmann, *et al.*, *New Journal of Physics* **13**, 045004 (2011).

[60] H. J. Mamin, *et al.*, *Science* **339**, 557 (2013).

[61] N. R. Parikh, *et al.*, *Applied physics letters* **61**, 3124–3126 (1992).

[62] C. F. Wang, E. L. Hu, J. Yang, J. E. Butler, *Journal of Vacuum Science & Technology B: Microelectronics and Nanometer Structures* **25**, 730 (2007).

[63] B. A. Fairchild, *et al.*, *Advanced Materials* **20**, 4793 (2008).

[64] M. Marchywka, P. E. Pehrsson, D. J. Vestyck, D. Moses, *Applied physics letters* **63**, 3521–3523 (1993).

[65] M. S. Dresselhaus, R. Kalish, *Ion implantation in diamond, graphite, and related materials* (Springer-Verlag, 1992).

[66] C. Uzan-Saguy, *et al.*, *Applied Physics Letters* **67**, 1194 (1995).

[67] Y. Tzeng, J. Wei, J. T. Woo, W. Lanford, *Applied physics letters* **63**, 2216–2218 (1993).

[68] P. Olivero, *et al.*, *Advanced Materials* **17**, 2427–2430 (2005).

[69] A. Reznik, V. Richter, R. Kalish, *Diamond and Related Materials* **7**, 317 (1998).

[70] M. Marchywka, P. E. Pehrsson, S. C. Binari, D. Moses, *Journal of The Electrochemical Society* **140**, L19 (1993).

[71] J. O. Orwa, K. W. Nugent, D. N. Jamieson, S. Prawer, *Physical Review B* **62**, 5461 (2000).

[72] G. d. Lange, Z. H. Wang, D. Ristè, V. V. Dobrovitski, R. Hanson, *Science* **330**, 60 (2010).

[73] B. Naydenov, *et al.*, *Applied Physics Letters* **97**, 242511 (2010).

[74] P. M. Martineau, *et al.*, *Journal of Physics: Condensed Matter* **21**, 364205 (2009).

[75] R. Locher, *et al.*, *Diamond and Related Materials* **6**, 654–657 (1997).

[76] J. Achard, *et al.*, *Journal of Physics D: Applied Physics* **40**, 6175 (2007).

[77] J. Stangl, V. Holý, G. Bauer, *Reviews of Modern Physics* **76**, 725 (2004).

[78] P. G. Baranov, *et al.*, *Small* **7**, 1533–1537 (2011).

[79] N. Gisin, G. Ribordy, W. Tittel, H. Zbinden, *Reviews of Moder Physics* **74**, 145 (2002).

[80] J. P. Goss, R. Jones, S. J. Breuer, P. R. Briddon, S. Öberg, *Physical Review Letters* **77**, 3041 (1996).

[81] H. Sternschulte, K. Thonke, R. Sauer, P. C. Münzinger, P. Michler, *Physical Review B* **50**, 14554 (1994).

[82] C. D. Clark, H. Kanda, I. Kiflawi, G. Sittas, *Physical Review B* **51**, 16681 (1995).

[83] I. Bayn, B. Meyler, J. Salzman, R. Kalish, *New Journal of Physics* **13**, 025018 (2011).

[84] A. C. Tamboli, M. C. Schmidt, A. Hirai, S. P. DenBaars, E. L. Hu, *Applied Physics Letters* **94**, 251116 (2009).

[85] J. Riedrich-Möller, *et al.*, *Nature Nanotechnology* **7**, 69 (2011).

[86] H. Okushi, H. Watanabe, S. Ri, S. Yamanaka, D. Takeuchi, *Journal of Crystal Growth* **237–239, Part 2**, 1269 (2002).

[87] Y. Akahane, T. Asano, B. S. Song, S. Noda, *et al.*, *Nature* **425**, 944–947 (2003).

[88] B.-S. Song, S. Noda, T. Asano, Y. Akahane, *Nature Materials* **4**, 207 (2005).

[89] S. Noda, M. Fujita, T. Asano, *Nature Photonics* **1**, 449 (2007).

[90] P. B. Deotare, M. W. McCutcheon, I. W. Frank, M. Khan, M. Loncar, *Applied Physics Letters* **94**, 121106 (2009).

[91] M. Khan, T. Babinec, M. W. McCutcheon, P. Deotare, M. Loncar, *Optics Letters* **36**, 421 (2011).

[92] C. Sauvan, G. Lecamp, P. Lalanne, J. Hugonin, *Optics Express* **13**, 245 (2005).

[93] M. Palamaru, P. Lalanne, *Applied Physics Letters* **78**, 1466 (2001).

[94] P. Lalanne, J. Hugonin, *IEEE Journal of Quantum Electronics* **39**, 1430 (2003).

[95] Y. Zhang, M. W. McCutcheon, I. B. Burgess, M. Loncar, *Optics Letters* **34**, 2694 (2009).

[96] T. van der Sar, *et al.*, *Applied Physics Letters* **98**, 193103 (2011).

[97] D. Englund, *et al.*, *Nano Letters* **10**, 3922 (2010).

[98] A. C. Scofield, *et al.*, *Nano Letters* **11**, 5387 (2011).

[99] L. Sekaric, *et al.*, *Applied Physics Letters* **81**, 4455 (2002).

[100] P. Ovartchaiyapong, L. M. A. Pascal, B. A. Myers, P. Lauria, A. C. Bleszynski Jayich, *Applied Physics Letters* **101**, 163505 (2012).

[101] Y. Tao, J. M. Boss, B. A. Moores, C. L. Degen, *arXiv:1212.1347* (2012).

[102] J. R. Maze, *et al.*, *Nature* **455**, 644 (2008).

[103] M. S. Grinolds, *et al.*, *Nature Physics* **7**, 687 (2011).

[104] I. Wilson-Rae, P. Zoller, A. Imamoglu, *Physical Review Letters* **92**, 075507 (2004).

[105] S. Kolkowitz, *et al.*, *Science* **335**, 1603 (2012).